EBERHARD-KARLS UNIVERSITÄT TÜBINGEN
MATHEMATISCH-NATURWISSENSCHAFTLICHE FAKULTÄT
FACHBEREICH PHYSIK

BACHELOR THESIS

Quantum Sensing beyond the Heisenberg Limit with the Boundary Time Crystal

Author:
Malik Jirasek

Supervisors:
Prof. Dr. Igor Lesanovsky
Dr. Albert Cabot

Referees:
Prof. Dr. Igor Lesanovsky

AG Lesanovsky
Institut für Theoretische Physik

July 15., 2025

Declaration of Authenticity

Hereby I declare that I wrote this work by myself and that I did not use any other aid or source than the ones indicated. All literal or logical quotes from other works I have marked as such. This work is not part of any other examination procedure - neither fully nor in parts. I have not published this work already - neither fully nor in parts.

Tübingen, July 15., 2025

_____   _____

Place, Date   Signature

Contents

List of Figures

List of Abbreviations

QFI quantum Fisher information

FI Fisher information

MPS matrix product state

cMPS continuous matrix product state

BTC continuous boundary time crystal

QCRB quantum Cramér Rao bound

CRB Cramér Rao bound

ME master equation

LME Lindblad master equation

i.i.d. independent and identically distributed

POVM positive operator-valued measure

LRBS low reflectivity beam splitter

HL Heisenberg limit

w.r.t. with respect to

HP Holstein-Primakoff

1. Introduction

Driven-dissipative many-body quantum systems can display collective behavior that enhances physical properties, resulting in outcomes that are more than the sum of their parts. Such collective behavior can lead to enhanced or suppressed emission characteristics [1, 2], or to the spontaneous breaking of time-translation symmetry in interacting nonequilibrium quantum systems. In the latter case, phases in which symmetry breaking occurs are referred to as time crystals [3–5]. A common feature of time crystal phases is the asymptotic oscillatory behavior of system observables [3–5], either with a period that is a discrete multiple of a given driving frequency [6–19], or by approaching a limit cycle under the influence of time-independent driving [20–34]. An example of the latter case is the continuous boundary time crystal (BTC) [20], emerging in driven-dissipative open quantum systems. It is realized in collective spin systems [20, 21], and experimentally observed in atom-cavity setups [35, 36], and in dense pencil-shaped atomic clouds [37].

The collective behavior observed in the BTC provides a platform for quantum sensing and metrology, where the driven-dissipative nature of the system acts as a constructive feature [38–40], rather than being detrimental to sensing protocols by destroying quantum correlations and adding noise to the system [41, 42]. The time crystal regime observed in the model used in this work displays strong quantum correlations, that become more pronounced with increasing system size [43]. These strong correlations motivate the implementation of the BTC as a quantum sensor [44]. The key element of this implementation is harnessing the information imprinted on the emission field through continuous monitoring of the BTC's output [38, 44–47]. On one hand, such monitoring can be achieved through standard protocols such as photon counting or homodyne detection [38, 45, 48–55]. On the other hand, protocols exist that leverage the correlations between a driven-dissipative quantum sensor and its emission field, by guiding the sensor output to an auxiliary quantum system, called a decoder [38, 46, 56]. Continuous monitoring of the decoder output can then improve measurement precision [46]. According to (quantum) parameter estimation theory, there exist fundamental bounds on such measurement protocols, quantified by the quantum Cramér Rao bound (QCRB) [42, 57, 58].

The goal of this thesis is to determine these fundamental bounds for the specific case of estimating an optical phase shift using a BTC as a resource for quantum enhanced sensing. In addition, measurement protocols enabling the detection of such a phase shift are analyzed.

This work is structured as follows: In Ch. 2, the framework of open quantum systems and matrix product states (MPS) is summarized, with application to the BTC model used throughout this work. This BTC is composed of N two-level systems and exhibits a transition from a stationary to a time crystal regime at a critical ratio of coherent driving to collective dissipation. This model is then investigated in the context of quantum sensing. Ch. 3 introduces the framework of (quantum) parameter estimation theory and applies it to the estimation of an optical phase shift φ imprinted on the emission field of a BTC. The quantum Fisher information (QFI) is computed using a deformed master equation (ME) and the MPS representation. The results follow the standard quantum limit for measurement time T, the Heisenberg limit (HL) with respect to the system size N in the stationary regime, and a super-HL scaling of N^4 in the time crystal regime. Ch. 4 then presents two measurement protocols that enable estimation of the optical phase shift φ. The first protocol is based on monitoring the output of a cascaded quantum system featuring a sensor BTC and an auxiliary decoder BTC. The second protocol involves monitoring the homodyne current of the sensor BTC. While the homodyne protocol does not show the advantage predicted by the QFI in the time crystal regime, the estimation error for the cascaded system protocol displays a scaling of up to $N^{-1.222}$ in the time crystal regime, thereby surpassing the HL. However, both the scaling of the QFI and the estimation error with system size come at the expense of increased coherent driving, which is required as the system size increases.

2. The Model

The theory of open quantum systems describes physical setups in which a subsystem interacts with an environment. In contrast to closed quantum systems, the subsystem can transfer energy and information to the environment. The framework of open quantum systems can be harnessed to efficiently describe sensors, where the emission field (the environment) of a quantum system (the subsystem) is monitored in order to estimate parameters of the quantum system [38, 44–47].

In this chapter, the model system on which this thesis is based is introduced. In Sec. 2.1, the framework of open quantum systems is explained using a ME representation and its relevant features for this work are highlighted. Sec. 2.2 introduces the BTC model employed throughout this work, highlighting its time-translation symmetry-breaking behavior in the thermodynamic limit. In Sec. 2.3, the representation of open quantum systems by MPS, which allows for simultaneous description of the system and environment evolution, is summarized.

2.1. Open Quantum Systems
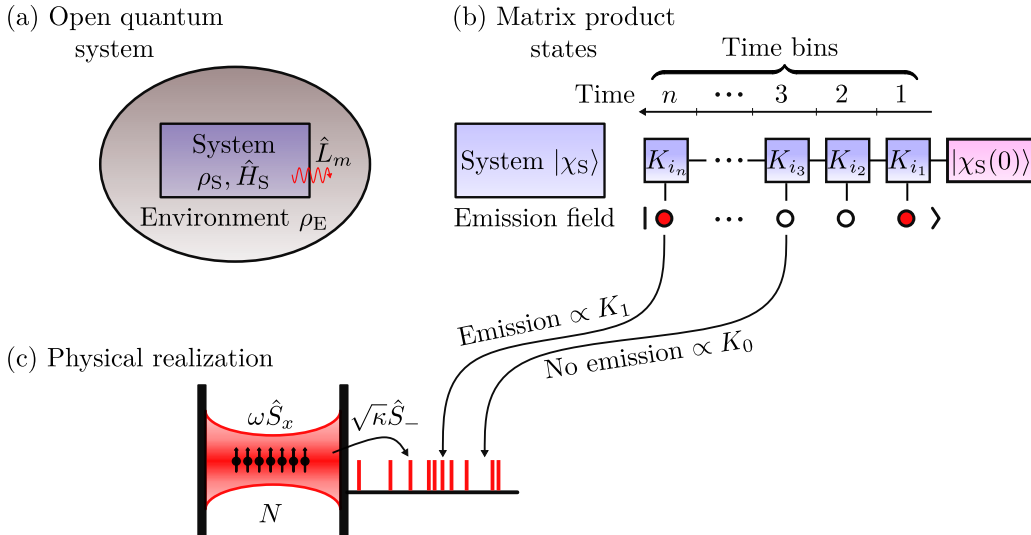
Figure 2.1: **Description of the BTC as an open quantum system.** (a) The BTC emerges in the system, a fraction of a larger setup containing also an environment of the system. The system is described by the state ρ_S and the Hamiltonian $\hat{H}_S$. The exchange of energy and information between the system and the environment is mediated by the jump operators $\hat{L}_m$, making it an open quantum system. The environment is described by the state ρ_E. (b) In a discrete-time description, the global state of the system and environment (here, the emission field) can be represented as a MPS, meaning that the interaction between the system and emission field is assumed to occur in discrete time bins of width δt. In this description, the emission field is composed of discrete time bin modes containing the emission record. For sufficiently small time bins, only single emissions per time bin are possible. The emission of a photon is mediated by application of K_1 to the system state and maps the time-bin mode from its vacuum (represented as a white filled dot in the emission field) to an occupied state (represented as a red filled dot in the emission field). The no-emission case is mediated by K_0, and the respective time bin remains in its vacuum. (c) A possible physical realization of a BTC is provided by N two-level systems in a cavity. The system is driven and dissipates into an emission field collectively, as described by the driving term $\omega \hat{S}_x$ and the jump operator $\sqrt{\kappa}\hat{S}_-$. Emission events, corresponding to the red dots in (b) are indicated by red dashes and occur only in a single direction, for example, as described by a waveguide. Adapted from [38].

The physical and statistical properties of the quantum systems considered in this work are characterized by their density matrix $\rho(t)$ at time t. The density matrix is a Hermitian, positive semi-definite operator with trace normalized to unity. The dynamics of the density matrix is defined by the von-Neumann equation

$$\partial_t \rho(t) = -\frac{i}{\hbar}[\hat{H}, \rho(t)], \tag{2.1}$$

with the Hamilton operator $\hat{H}$ of the quantum system. The convention $\hbar = 1$ is used throughout. The density matrix allows to calculate expectation values of system observables $\mathcal{O}$ according to

$$\langle \mathcal{O} \rangle (t) = \text{Tr}[\mathcal{O}\rho(t)] \tag{2.2}$$

where $\langle \bullet \rangle$ denotes expectation values in the state of the quantum system.

Open quantum systems emerge when a quantum system can be partitioned into at least two subsystems. A common case is the partition into a system of interest S (called the system throughout for simplicity) and an environment E. The interaction between these subsystems renders S an open quantum system. If one is only interested in the behavior of one of the subsystems, the behavior of the other can be averaged out by tracing over the respective degrees of freedom. This yields the reduced density matrix of the system, $\rho_S = \text{Tr}_E[\rho]$, and the environment, $\rho_E = \text{Tr}_S[\rho]$, where Tr_i denotes the partial trace over subsystem i. The evolution of the respective subsystems depends on the physical setup of system and environment chosen, and especially on their interactions. In typical scenarios of quantum optics, the evolution of the reduced system density matrix is determined by a Lindblad master equation (LME) or Markovian ME

$$\partial_t \rho_S(t) = -i[\hat{H}_S, \rho_S(t)] + \mathcal{D}[\rho_{\mathcal{S}}(t)] =: \mathcal{L}[\rho_S(t)], \tag{2.3}$$

with the dissipator $\mathcal{D}[\bullet] = \sum_{m=1}^{M}[\hat{L}_m \bullet \hat{L}_m^\dagger - \{\hat{L}_m^\dagger\hat{L}_m, \bullet\}/2]$. Here $\hat{H}_S$ is a Hamilton operator describing the coherent evolution of the system and $\hat{L}_m$ are jump operators describing potential dissipative behavior of the system. The object $\mathcal{L}$ is the Lindblad superoperator that generates the time evolution of the density matrix [59, 60]. Eq. (2.3) describes Markovian dynamics, meaning that the Born-Markov approximation of weak system-environment interactions and fast decaying environment correlations is justified [59, 60]. Formal solutions of Eq. (2.3) can be written as

$$\rho_S(t) = e^{t\mathcal{L}}\rho_S(0). \tag{2.4}$$

2.2. The continuous Boundary Time Crystal

The model employed throughout this work is an ensemble of N two-level emitters interacting with an electromagnetic emission field and described by the LME

$$\partial_t \rho_S = \mathcal{L}[\rho_S] = -i\omega[\hat{S}_x, \rho_S] + \kappa \left(\hat{S}_- \rho_S \hat{S}_+ - \frac{1}{2}\{\hat{S}_+\hat{S}_-, \rho_S\} \right). \tag{2.5}$$

$\hat{S}_\alpha = \sum_{i=1}^{N} \sigma_\alpha^i/2$, with $\alpha \in \{x, y, z\}$, are collective total angular momentum operators, where the Pauli matrices σ_α^i correspond to emitter i, and the ladder operators are $\hat{S}_\pm = \hat{S}_x \pm i\hat{S}_y$. The set of jump operators $\hat{L}_m$ thus reduces to the single jump operator $\hat{L} = \sqrt{\kappa}\hat{S}_-$, and the Hamiltonian reads $\hat{H}_S = \omega\hat{S}_x$. Such an LME emerges in the description of atoms in a cavity driven by a laser with Rabi frequency ω, collectively decaying and emitting photons out of the cavity with rate κ. It originates from the description of cooperative resonance fluorescence [43, 61, 62], and can also be derived as an edge case of a transverse field Ising model [63].
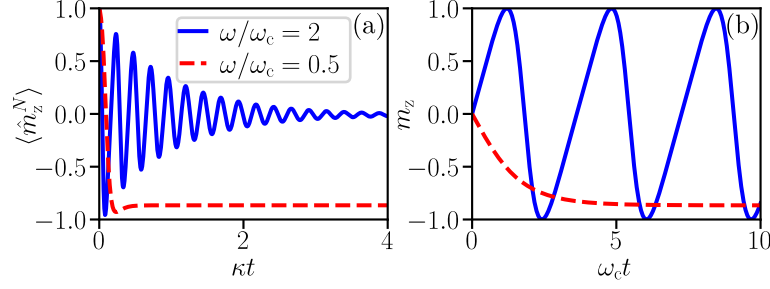
Figure 2.2: **Mean-field expectation values for the BTC.** (a) Mean-field expectation value $\langle \hat{m}_{\mathrm{z}}^{N} \rangle$ for $N = 30$ in the stationary regime for $\omega/\omega_{\mathrm{c}} = 0.5$ (red dashed line) and in the time crystal regime for $\omega/\omega_{\mathrm{c}} = 4$ (blue solid line). Time is given in units κ and the initial conditions are $\langle \hat{S}^2 \rangle = (N/2)^2$ and $\langle \hat{S}_{\mathrm{z}} \rangle = N/2$. (b) Mean-field expectation value m_{z} in the thermodynamic limit $N \to \infty$ in the stationary regime for $\omega/\omega_{\mathrm{c}} = 0.5$ (red dashed line) and in the time crystal regime for $\omega/\omega_{\mathrm{c}} = 4$ (blue solid line). Time in units of the critical frequency ω_{c}, with initial conditions $(m_{\mathrm{x}}, m_{\mathrm{y}}, m_{\mathrm{z}}) = (0, 1, 0)$.

The system-environment setup described by Eq. (2.5) is a driven-dissipative model displaying collective nonequilibrium behavior, which can be revealed by counting statistics of emitted photons [43] or by continuous measurement protocols [64, 65]. Eq. (2.5) conserves the total angular momentum, such that the simultaneous eigenbasis of $\hat{S}^2$ and $\hat{S}_{\mathrm{z}}$ is the natural basis for the Hilbert space of the system S. In this work, initial conditions restricted to the maximum total angular momentum $S = N/2$ are assumed. With this assumption, a phase transition can be observed for large system sizes at the critical Rabi frequency $\omega_{\mathrm{c}} = N\kappa/2$.

For $\omega < \omega_{\mathrm{c}}$, referred to as the stationary regime, the system rapidly approaches a stationary state via overdamped relaxation. The stationary state in this regime is essentially a coherent state of the ladder operator, as shown by [43, 66] and in Sec. A.3. For $\omega > \omega_{\mathrm{c}}$, the system displays oscillatory behavior, enveloped by a slow decay towards a stationary state for finite N. With increasing system size, this oscillatory behavior becomes more pronounced, and in the thermodynamic limit $N \to \infty$, persistent oscillations with well-defined frequency and amplitude emerge. Such oscillatory behavior can be observed in the mean-field expectation values (see Fig. 2.2) with the mean-field operators $\hat{m}_{\alpha}^{N} = 2\hat{S}_{\alpha}/N$, which converge to multiples of the identity in the thermodynamic limit: $\lim_{N \to \infty} \hat{m}_{\alpha}^{N} = \lim_{N \to \infty} \langle \hat{m}_{\alpha}^{N} \rangle =: m_{\alpha}$ [21, 67, 68]. Due to its time-translation symmetry-breaking nature this regime is referred to as the time crystal regime. Note that, in order to obtain a well-defined thermodynamic limit, the decay rate should be rescaled as $\kappa \to 2\kappa/N$ [20, 21, 39]. In this work, however, the scope is on finite-size systems and a N-independent rate κ is considered, allowing for a close connection of the model Eq. (2.5) to experimental setups [37]. Nevertheless, the critical driving ω_{c} is linearly dependent on N, so that the analysis of a point in the phase diagram with a fixed value of $\omega/\omega_{\mathrm{c}}$ requires a stronger driving ω with increasing system size N. Effectively, this means that the Rabi frequency can become an extensive parameter, which is accounted for by rescaling $\omega = N\tilde{\omega}/2$, with an intensive parameter $\tilde{\omega}$ [38].

As the time crystal regime emerges in a driven-dissipative open quantum system, this system can be understood as a continuous boundary time crystal (BTC) [20]. Such a model and phase transition are experimentally realized with atom-cavity setups [35, 36] or dense pencil-shaped atomic clouds [37].

2.3. Matrix Product States

In this work, open quantum systems are investigated in the context of quantum sensing, by monitoring their environment. In the model of Sec. 2.2, this is the output field of photons emitted by a BTC. A convenient description in such a situation is the matrix product state (MPS) representation of the joint system and environment state. For a system and environment obeying Eq. (2.3), when tracing out the environment, the joint evolution of system and environment can be discretized to short but finite time bins of size δt. The global state of system and environment

at time $T = n\delta t$ then is the MPS [44, 47, 69]

$$|\psi(T)\rangle = \sum_{i_1,\ldots,i_n=0}^{M} K_{i_n}\ldots K_{i_1} |\chi_\mathrm{S}\rangle \otimes |i_1,\ldots,i_n\rangle, \tag{2.6}$$

with the Kraus operators

$$K_0 = e^{-i\delta t\hat{H}_\mathrm{S}}\sqrt{1 - \delta t\sum_{m=1}^{M}\hat{L}_m^\dagger\hat{L}_m} = 1 - i\delta t\hat{H}_\mathrm{S} - \frac{\delta t}{2}\sum_{m=1}^{M}\hat{L}_m^\dagger\hat{L}_m + \mathcal{O}(\delta t^2),$$
$$K_{i>0} = e^{-i\delta t\hat{H}_\mathrm{S}}\sqrt{\delta t}\hat{L}_i = \sqrt{\delta t}\hat{L}_i + \mathcal{O}(\delta t^{3/2}), \tag{2.7}$$

where, in the following, only contributions up to order $\mathcal{O}(\delta t)$ are considered. The environment state $|i_1,\ldots,i_n\rangle$ is the record of quantum jumps mediated by the respective jump operators and $|\chi_\mathrm{S}\rangle$ is the initial state of the system. $i_j > 0$ indicates a jump at time $j\delta t$ mediated by $\hat{L}_{i_j}$, while $i_j = 0$ corresponds to the no-jump scenario.

Such evolution can be compared to the sequential interaction of a system with discretized time bin modes initialized in the vacuum $|0_j\rangle$ before the interaction, and mapped to the output state $|i_j\rangle$, with the system updated according to K_{i_j} [69]. A similiar result can be obtained employing a collision model [70] and emerges as a coarse grained description of the unitary joint evolution of system and environment [39]. In the limit $\delta t \to 0$, the global state emerges as a continuous matrix product state (cMPS) [71, 72] and one recovers the LME under tracing out the environment degrees of freedom, such that

$$\lim_{\delta t\to 0}\mathrm{Tr}_\mathrm{E}\left[|\psi(T)\rangle\langle\psi(T)|\right] = e^{T\mathcal{L}}\rho_\mathrm{S}(0). \tag{2.8}$$

For the BTC the Kraus operators simplify to

$$K_0 = 1 - i\delta t\omega\hat{S}_\mathrm{x} - \frac{\kappa\delta t}{2}\hat{S}_+\hat{S}_- + \mathcal{O}(\delta t^2),$$
$$K_1 = \sqrt{\kappa\delta t}\hat{S}_- + \mathcal{O}(\delta t^{3/2}), \tag{2.9}$$

with $i_j \in \{0,1\}$ simply counting whether or not a photon is detected in the time bin j.

3. Parameter Estimation Theory

A general interest in (quantum) metrology is to define and analyze the fundamental bounds of precision for parameter estimation. A key element in parameter estimation theory is the (quantum) Cramér Rao bound (CRB) —an inequality which gives an upper bound on the estimation precision of any measurement. As will be explained, the defining quantity in this inequality is the (quantum) Fisher information (FI).

In this chapter, the theoretical framework of parameter estimation is summarized in Sec. 3.1 for classical measurements. In Sec. 3.2, these ideas are then extended to the case of measurements with quantum systems. Finally, in Sec. 3.3, this theoretical framework is applied to the estimation of an optical phase shift imprinted on photons emitted by a BTC (see Sec. 2.2). An expression for the QFI is derived and numerically computed following two different approaches. The first approach (see Sec. 3.3.1) uses a deformed master equation (ME) to determine the QFI, whereas the second approach (see Sec. 3.3.2) is based on the representation of the global system and environment state as a MPS. Numerical results are presented in Sec. 3.3.1 and in Sec. 3.3.2. The motivations and derivations of this chapter are based on [44, 47, 57, 58].

3.1. Classical Parameter Estimation

The problem of parameter estimation can be formulated as follows: In a first step, a system is prepared and a measurement apparatus is initialized. After the preparation of the system in its initial state, it evolves according to dynamics involving the physical parameter θ. The parameter θ is thus imprinted on the state of the system. In a second step, the system is coupled to the measurement apparatus and a measurement is performed. The outcome of the measurement is recorded and is, in general, a random classical variable. The question then is: how accurately can the value of the parameter θ be estimated from the measurement outcome(s)?

Throughout this work, a statistical perspective on the measurement procedure is taken, such that the single measurement outcomes are interpreted as samples of an underlying probability distribution. The main difference between the classical case and the quantum case is the nature of the distribution of measurement outcomes which is classical in the former case and has quantum features in the latter case.

By monitoring the outcomes of n repeated measurements of a given system, information about the probability distribution $p(\vec{x})$ of the possible measurement outcomes $(x_1, \ldots, x_M) = \vec{x}$ is collected. The state of the system and therefore also the distribution p depends on the parameter θ of the system, so that the distribution is a conditioned distribution $p(\vec{x}|\theta)$. This distribution is an element of the model $\mathcal{P} = \{p(\cdot|\theta) : \theta \in \Theta\}$ where Θ is the set of all possible parameters. To estimate the system parameter θ an estimator $\hat{\theta}(\vec{x})$ is computed. The precision with which the parameter θ can be estimated by the estimator $\hat{\theta}$ is now fundamentally limited by the sensitivity of the model $\mathcal{P}$ to changes in θ. A measure of this sensitivity is given by the Fisher information (FI) defined as

$$I(\theta) := \mathbb{E}_\theta \left[(\partial_\theta \ln p(\vec{x}|\theta))^2 \right].$$ (3.1)

In the above definition, $\mathbb{E}_\theta$ denotes the expectation value with the distribution $p(\vec{x}|\theta)$ evaluated at θ. Under the conditions given in [57], a lower bound —the Cramér Rao bound (CRB) —on the variance of any unbiased estimator, that means any estimator satisfying $\mathbb{E}_\theta[\hat{\theta}(\vec{x}) - \theta] = 0$, can be determined. It is given by

$$\text{Var}_\theta[\hat{\theta}] \geq \frac{1}{I(\theta)}.$$ (3.2)

Here, Var_θ indicates that the variance is evaluated with the distribution $p(\vec{x}|\theta)$, at parameter value θ. The variance of such an unbiased estimator is interpreted as the measurement precision when estimating the parameter θ using $\hat{\theta}$ in the following. Under the assumption of independent and identically distributed (i.i.d.) variables, one finds for a sequence of M measurements that $I(\theta) = M I_1(\theta)$, where I_1 refers to the FI of a single measurement, implying that the limit on the measurement precision decreases as $1/M$.

Note that the distribution $p(\vec{x}|\theta)$ is determined from a sample of measurement outcomes and therefore depends on the type of measurement chosen. Consequently, the FI also depends on the type of measurement chosen and thus only defines a limit on the precision of a given type of measurement.

3.2. Quantum Parameter Estimation

Until now, the nature of the probability distribution p is not specified. This changes in the following section. Measurement setups where the environment of an open quantum system is monitored are the scope of this work. In such a case all properties of the system and environment at the measurement time T are described by the global density matrix $\rho(T)$. The measurement of general outcomes ξ is described by a positive operator-valued measure (POVM), $\{\hat{E}_\xi\}$. As the evolution of the system depends on the parameter θ, the density matrix $\rho(T, \theta)$ generally also depends on θ. The probability of a certain measurement outcome ξ is then given by

$$p(\xi, T|\theta) = \text{Tr}\left[\rho(T, \theta)\hat{E}_\xi\right]. \tag{3.3}$$

As can be seen from the above equation for the probability distribution, a particular difficulty in computing the FI for a given measurement arises from taking the derivative of the probability distribution with respect to (w.r.t.) θ. This reduces to the derivative of the density matrix which can—at least formally —be written as

$$\frac{d\rho(T, \theta)}{d\theta} = \frac{1}{2}\left(\mathcal{D}_\theta \rho(T, \theta) + \rho(T, \theta)\mathcal{D}_\theta\right). \tag{3.4}$$

The operator $\mathcal{D}_\theta$ is called the symmetric logarithmic derivative and in general a solution for the above equation is hard to compute. If $\mathcal{D}_\theta$ is known, then the FI optimized over all possible measurements $\{\hat{E}_\xi\}$, called the quantum Fisher information (QFI), is given by [47, 73–76]

$$F(\theta) = \text{Var}_\theta\left[\mathcal{D}_\theta\right]. \tag{3.5}$$

In the case of a measurement with a quantum system the variance of any unbiased estimator $\hat{\theta}$ is lower bounded as described by the quantum Cramér Rao bound (QCRB)

$$\text{Var}_\theta[\hat{\theta}] \geq \frac{1}{I(\theta)} \geq \frac{1}{F(\theta)}, \tag{3.6}$$

similar to Eq. (3.2). The second inequality is due to $I(\theta) < F(\theta)$. Since the QFI is optimized over all possible measurements and solely depends on the state $\rho(T, \theta)$, it gives an upper bound to the FI extractable by a given measurement. The sensing of a given parameter θ thus translates to a twofold problem. On the one hand, a system that yields a high QFI has to be found. On the other hand, measurement protocols saturating the QCRB with $I(\theta) = F(\theta)$ need to be applied in order to reach the best possible precision. In this context a measurement protocol saturating the QCRB is called optimal in the following.

For general density matrices $\rho(T, \theta)$, the QFI can be challenging to compute analytically. In the case of a pure state $\rho(T, \theta) = |\psi_\theta\rangle\langle\psi_\theta|$, the QFI takes the convenient form [41]

$$\begin{aligned}
F(T, \theta) &= 4(\langle\psi'_\theta|\psi'_\theta\rangle - |\langle\psi'_\theta|\psi_\theta\rangle|^2) \\
&= 4\partial_{\theta_1}\partial_{\theta_2}\ln\langle\psi_{\theta_1}|\psi_{\theta_2}\rangle\big|_{\theta_1=\theta_2=\theta}.
\end{aligned} \tag{3.7}$$

Here, $|\psi'_\theta\rangle$ denotes the derivative $\partial_\theta |\psi_\theta\rangle$. This means that the defining quantity for the QFI for a pure state is the fidelity $\mathcal{F}(T, \theta_1, \theta_2) = \langle \psi_{\theta_1} | \psi_{\theta_2} \rangle$, where $|\psi_{\theta_i}\rangle$ are states evaluated at arbitrary positions θ_i in parameter space. For $\theta_i \to \theta$ they resemble physical states.

If in addition —as explained in the next section —the parameter is imprinted by a generator $\hat{G}$ via a unitary transformation as $|\psi_\theta\rangle = e^{-i\theta\hat{G}} |\psi\rangle$, the QFI simplifies to [41]

$$F(T, \theta) = 4(\langle \psi_\theta | \hat{G}^2 | \psi_\theta \rangle - \langle \psi_\theta | \hat{G} | \psi_\theta \rangle^2) = 4 \operatorname{Var}_\theta[\hat{G}]. \tag{3.8}$$

In most practical cases, as well as in this work, the resources for preparing and monitoring the physical system carrying the parameter θ are defined by the system size N (for example, the number of contributing particles) and the measurement time T. In this context, an asymptotic scaling behavior of the QFI with $F \propto TN$ is called the standard quantum limit. It is, for example, realized if the state of the system is a product state of N uncorrelated constituents. If, in contrast, the state of the system features correlations or if the system displays a phase transition, the QFI can scale as $F \propto T^\alpha N^\beta$ with $\alpha, \beta \geq 1$. An asymptotic scaling where either $\alpha = 2$ or $\beta = 2$ is called the HL regarding the respective resource [41, 45, 47].
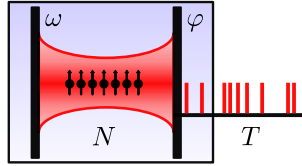
3.3. Estimation of an Optical Phase Shift

Figure 3.1: **Phase shift φ, imprinted on the photons emitted by a BTC.** The emission field acquires a phase φ, which leads to a transformation of the jump operator. The Rabi frequency ω, the system size N and the measurement time T are known and the parameter φ is to be estimated. Adapted from [38].

In this section, the QFI is computed for the estimation of an optical phase shift φ, imprinted on the photons emitted by a BTC, as described in Sec. 2.2 and sketched in Fig. 3.1. According to [47], the underlying transformation that describes the optical phase shift can be traced to the jump operators as

$$\hat{L} = \sqrt{\kappa}\hat{S}_- \to \hat{L}_\varphi = \sqrt{\kappa}\hat{S}_- e^{-i\varphi}. \tag{3.9}$$

The parameter to be estimated is therefore φ, replacing θ in the above derivations. The transformation of the jump operator directly implies a similar transformation of the Kraus operators in the MPS description, as

$$K_0 \to K_{0,\varphi} = K_0, \; K_1 \to K_{1,\varphi} = \sqrt{\kappa\delta t}\hat{S}_- e^{-i\varphi} = K_1 e^{-i\varphi}. \tag{3.10}$$

This structure of the Kraus operators allows the formulation of the global system and environment MPS in terms of the generator $\Lambda(T)$, as [47]

$$|\psi_\varphi\rangle = \sum_{i_1,\ldots,i_n=0}^1 K_{i_n,\varphi} \ldots K_{i_1,\varphi} |\chi_S\rangle \otimes |i_1,\ldots,i_n\rangle = e^{-i\varphi\Lambda(T)} |\psi\rangle, \tag{3.11}$$

with the system initial state $|\chi_S\rangle$ and the emission field time record $|i_1,\ldots,i_n\rangle$. Here, $\Lambda(T)$ counts the number of quantum jumps mediated by K_1 until time $T = n\delta t$. In other words, $\Lambda(T)$ is the time integrated photon count at time T. As shown in the following, the generator $\Lambda(T)$ links the parameter estimation problem treated here to a photon counting problem, and since the QFI is the variance of the generator Λ, it inherits the properties of the counting statistics of a single BTC.

3.3.1. Deformed Master Equation approach

In this subsection, the QFI is determined by computing the fidelity presented in Eq. (3.7). Using the MPS description, the fidelity reads

$$
\begin{aligned}
\mathcal{F}(T, \varphi_2, \varphi_1) &= \langle \psi_{\varphi_2} | \psi_{\varphi_1} \rangle \\
&= \sum_{\substack{i_1, \ldots, i_n = 0 \\ i'_1, \ldots, i'_n = 0}}^{1} \langle \chi_{\mathrm{S}} | K^{\dagger}_{i'_1, \varphi_2} \ldots K^{\dagger}_{i'_n, \varphi_2} K_{i_n, \varphi_1} \ldots K_{i_1, \varphi_1} | \chi_{\mathrm{S}} \rangle \langle i'_1, \ldots, i'_n | i_1, \ldots, i_n \rangle \\
&= \mathrm{Tr}_{\mathrm{S}} \left[\underbrace{\sum_{i_1, \ldots, i_n = 0}^{1} K_{i_n, \varphi_1} \ldots K_{i_1, \varphi_1} | \chi_{\mathrm{S}} \rangle \langle \chi_{\mathrm{S}} | K^{\dagger}_{i_1, \varphi_2} \ldots K^{\dagger}_{i_n, \varphi_2}}_{=: \rho_{\mathrm{S}}^{\varphi_1, \varphi_2}(T)} \right].
\end{aligned}
\tag{3.12}
$$

The definition of $\rho_{\mathrm{S}}^{\varphi_1, \varphi_2}$ is such that when $\varphi_1 = \varphi_2 = \varphi$, the physical density matrix of the system is recovered. For $\varphi_1 \neq \varphi_2$, $\rho_{\mathrm{S}}^{\varphi_1, \varphi_2}$ is not a physical density matrix, and thus does not obey a time evolution according to a LME. However, the time evolution can be determined by taking the limit of infinitesimal δt, similar to Sec. 2.3. The result is the deformed ME

$$
\partial_t \rho_{\mathrm{S}}^{\varphi_1, \varphi_2} = -i \left[\hat{H}_{\mathrm{S}}, \rho_{\mathrm{S}}^{\varphi_1, \varphi_2} \right] + \hat{L}_{\varphi_1} \rho_{\mathrm{S}}^{\varphi_1, \varphi_2} \hat{L}^{\dagger}_{\varphi_2} - \frac{1}{2} \left\{ \hat{L}^{\dagger}_{\varphi_1} \hat{L}_{\varphi_1} \rho_{\mathrm{S}}^{\varphi_1, \varphi_2} + \rho_{\mathrm{S}}^{\varphi_1, \varphi_2} \hat{L}^{\dagger}_{\varphi_2} \hat{L}_{\varphi_2} \right\}
\tag{3.13}
$$

$$
= \mathcal{L} \left[\rho_{\mathrm{S}}^{\varphi_1, \varphi_2} \right] + \left(e^{-i(\varphi_1 - \varphi_2)} - 1 \right) \hat{S}_{-} \rho_{\mathrm{S}}^{\varphi_1, \varphi_2} \hat{S}_{+}
\tag{3.14}
$$

$$
=: \mathcal{L}_{\Delta\varphi} \left[\rho_{\mathrm{S}}^{\Delta\varphi} \right],
\tag{3.15}
$$

where in Eq. (3.15) $\varphi_1 - \varphi_2 =: \Delta\varphi$ and the deformed Lindbladian $\mathcal{L}_{\Delta\varphi}$ is defined similarly to the physical Lindbladian. Since Eq. (3.14) only depends on the phase difference $\Delta\varphi$, the density matrix and the deformed Lindbladian also only depend on $\Delta\varphi$ as indicated in Eq. (3.15). The Hamiltonian $\hat{H}_{\mathrm{S}}$ is independent of $\Delta\varphi$ and thus is the same as the physical Hamiltonian. In the limit $\Delta\varphi = 0$, the physical Lindbladian $\mathcal{L}$ emerges from the deformed Lindbladian. Interestingly, the deformed ME is directly connected to a large deviations approach to photocounting as noted in [47]. A tilted ME generated by the tilted Lindbladian $\tilde{\mathcal{L}}_s = \mathcal{L}_{\Delta\varphi = -is}$, is used in [77] to determine the statistics of quantum jumps. Here, these quantum jumps are related to the emission of photons and thus, up to a phase, Eq. (3.15) generates the moments of the photon emission statistics. The long time limit of both the fidelity and the photon count statistics is described by the eigenvalue $\lambda_0(\Delta\varphi)$ of $\mathcal{L}_{\Delta\varphi}$ with the largest real part [44, 47, 77]

$$
\bar{F}_{\varphi} := \lim_{T \to \infty} \frac{F(T, \varphi)}{T} = 4 \partial_{\varphi_1} \partial_{\varphi_2} \lambda_0(\Delta\varphi) \big|_{\Delta\varphi = 0}.
\tag{3.16}
$$

An immediate consequence of Eq. (3.16) is that the QFI asymptotically scales linearly with measurement time T. Also, this equation is a powerful numerical tool because the dominant eigenvalues of the deformed Lindbladian can be efficiently computed numerically for intermediate system sizes of $N \sim 100$. A sample of the numerical results is shown in Fig. 3.2.

The numerical results in Fig. 3.2 show a sharp transition of the QFI at the critical point $\omega = \omega_{\mathrm{c}}$, which becomes more prominent with increasing system size. In the stationary regime, the QFI can be computed by determining the dominant eigenvalue of the deformed Lindbladian using a Holstein-Primakoff (HP) approach (see Sec. A.3 and [38] for a detailed derivation), yielding

$$
\bar{F}_{\varphi} = 4 \frac{\omega^2}{\kappa}.
\tag{3.17}
$$

This expression shows a quadratic dependence of the QFI on the Rabi frequency and matches the numerical results when the QFI is evaluated in the stationary regime and not too close to the critical

frequency ω_c. Note, that due to the rescaling $\omega = N\tilde{\omega}/2$, this expression scales quadratically with N, assuming that the Rabi frequency is increased as the system size increases.
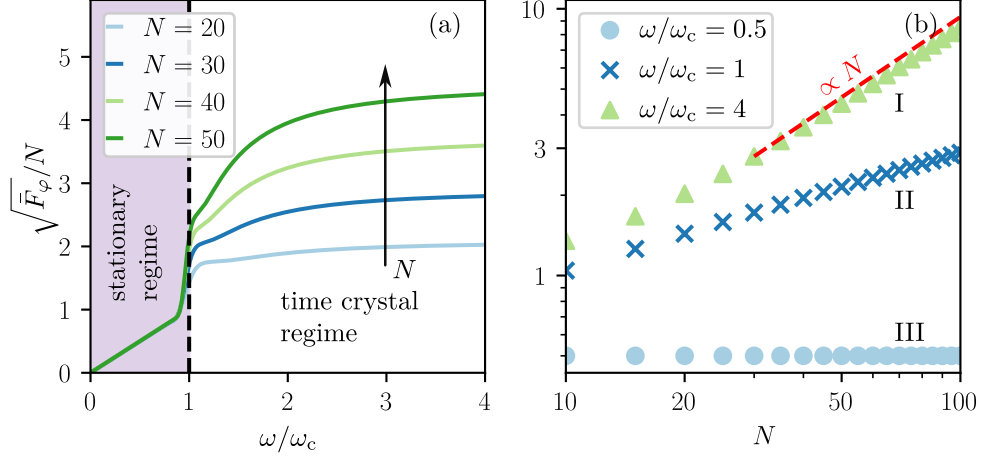

Figure 3.2: **Numerical results for the QFI in the deformed ME description.** (a) Square root of the QFI as described by Eq. (3.16) and rescaled by the system size N as a function of the Rabi frequency ω. (b) Square root of the QFI as described by Eq. (3.16) and rescaled by the system size N as a function of the system size for selected points in the phase diagram. For I and II the asymptotic behavior is determined by a power law fit yielding scaling behaviors of $\bar{F}_\varphi \propto N^{\alpha_i}$ with $\alpha_\mathrm{I} = 3.923 \pm 0.004$ and $\alpha_\mathrm{II} = 2.8417 \pm 0.0018$. For III the QFI is well described by Eq. (3.17) and displays a scaling $\propto N^2$.

In the time crystal regime, the QFI saturates with increasing Rabi frequency. As pointed out in [38], this shows that changes in the Rabi frequency and in the system size have distinct effects on the QFI, and thus the observed scaling behavior of the QFI in the time crystal regime is a many-body effect. In fact, these many-body effects lead to an intriguing scaling close to $\bar{F}_\varphi \propto N^4$, beyond the HL. The cost for this scaling is an increase in the Rabi frequency $\omega = N\tilde{\omega}/2$ required to remain in the time crystal regime.

The many-body enhancement of the QFI has several reasons. First, the close connection between the estimation problem and the counting problem implies that the QFI shares the properties of the photon emission behavior of the system. In the chosen model, the emission of a photon is already a collective process, such that in both the stationary and time crystal regime, a many-body enhancement of the QFI can be observed. Second, as pointed out in [64], the oscillatory behavior of the system in the time crystal regime translates directly into an oscillatory detection signal of the emission field, implying strong correlations between the system and the emission field. As pointed out in [64, 78], the stationary state of the system in the time crystal regime is close to the maximally mixed state, which also hints at such strong correlations, leading to an advantage over the stationary regime. Third, according to [21, 23, 43, 64], the quality and amplitude of the observed oscillations increases with increasing system size, such that the oscillatory behavior of the emission field becomes more defined in its frequency and has a higher contrast to noise. In order to understand the advantage of the QFI in the time crystal regime over the stationary regime in more detail and motivated by the results of [44, 46, 47], the notion of strong correlations as a signal for an enhanced QFI is analyzed in the next section.

3.3.2. Matrix Product State approach

In contrast to Sec. 3.3.1, the QFI is computed here by determining the derivative of the MPS in Eq. (3.7), leading to an alternative expression than Eq. (3.16). With the transformation given in

Eq. (3.10) at hand, the derivative reads

$$|\psi_\varphi'\rangle = \partial_\varphi |\psi_\varphi\rangle = \sum_{i_1,\dots,i_n=0}^{1} \sum_{j=1}^{n} K_{i_n}\dots(\partial_\varphi K_{i_j})\dots K_{i_1} |\chi_{\mathrm{S}}\rangle \otimes |i_1,\dots,i_n\rangle, \tag{3.18}$$

with $T = n\delta t$. As one can see, the derivative w.r.t. φ acts on all time bins. Thus, the inner products appearing in Eq. (3.7) have contributions where the derivative acts on the same time bin for both the bra and the ket vector and contributions where the derivative acts on different time bins, respectively. Only terms where the derivative acts on the Kraus operator K_1 contribute since K_0 is independent of φ. Computing the inner products explicitly yields

$$\langle\psi_\varphi|\psi_\varphi'\rangle = \sum_{j=1}^{n} \mathrm{Tr}\Big[\rho_{\mathrm{S}}(t_{j-1})(-i\kappa\delta t)\hat{S}_+\hat{S}_-\Big] \overset{\delta t\to 0}{\longrightarrow} -i\kappa \int_0^T dt\, \mathrm{Tr}\Big[\rho_{\mathrm{S}}(t)\hat{S}_+\hat{S}_-\Big], \tag{3.19}$$

$$\langle\psi_\varphi'|\psi_\varphi'\rangle = \sum_{j=1}^{n} \mathrm{Tr}\Big[\rho_{\mathrm{S}}(t_{j-1})\kappa\delta t\hat{S}_+\hat{S}_-\Big] + 2\sum_{j>k=1}^{n} \mathrm{Tr}\Big[(\kappa^2\delta t^2)\hat{S}_+\hat{S}_-(\hat{S}_-\rho_{\mathrm{S}}(t_{k-1})\hat{S}_+)(\tau)\Big] \tag{3.20}$$

$$\overset{\delta t\to 0}{\longrightarrow} \kappa\int_0^T dt\, \mathrm{Tr}\Big[\rho_{\mathrm{S}}(t)\hat{S}_+\hat{S}_-\Big] + 2\kappa^2\int_0^T dt\int_0^{T-t} d\tau\, \mathrm{Tr}\Big[\hat{S}_+\hat{S}_- e^{\mathcal{L}\tau}(\hat{S}_-\rho_{\mathrm{S}}(t)\hat{S}_+)\Big], \tag{3.21}$$

where, in Eq. (3.20), the definition $\tau := t_{j-1} - t_{k+1}$ is made and the limit of infinitesimally small time bins is taken. $\rho_{\mathrm{S}}(t)$ is the density matrix of the system obtained when tracing out the environment. A more detailed calculation can be found in Sec. A.1. As seen in Sec. 3.3.1, there is a close link between the estimation problem and the photon counting problem. This also manifests in Eq. (3.21) and Eq. (3.19), as the latter is just (up to a phase) the time integrated average intensity and the former is the two-time intensity correlation [58].

In the scope of this work, long measurement times T are considered and thus it is assumed that the state of the system $\rho_{\mathrm{S}}(t)$ can be approximated by the stationary state ρ_{ss} of the Lindbladian $\mathcal{L}$ everywhere under the integrals, such that

$$F(T,\varphi) = 8\kappa^2 \int_0^T dt\int_0^{T-t} d\tau\, C_{S_+,S_-}^{S_-,S_+}(\tau) + 4\kappa T\,\langle\hat{S}_+\hat{S}_-\rangle_{\mathrm{ss}} - 4\kappa^2 T^2\,\langle\hat{S}_+\hat{S}_-\rangle_{\mathrm{ss}}^2, \tag{3.22}$$

where the two-time correlations are defined as $\mathrm{Tr}\Big[\hat{O}_1\hat{O}_2 e^{\mathcal{L}\tau}(\hat{O}_3\rho_{\mathrm{ss}}\hat{O}_4)\Big] =: C_{O_1,O_2}^{O_3,O_4}(\tau)$ and expectation values of operators $\hat{O}$ in the stationary state read $\langle\hat{O}\rangle_{\mathrm{ss}} = \mathrm{Tr}\Big[\hat{O}\rho_{\mathrm{ss}}\Big]$. Interesting behavior of the QFI can also unfold for short measurement times, as pointed out in [47], but is not further investigated here. The pivotal point now is to determine the two-time correlations, as those capture potential collective behavior that can lead to the enhancement of the QFI seen in the previous section.

In the stationary regime ($\omega < \omega_{\mathrm{c}} = N\kappa/2$), one finds that the stationary state of the system is, in leading order of the system size N, given by a coherent state of the jump operator, such that $\rho_{\mathrm{ss}} = |E_0\rangle\langle E_0|$ with $\hat{S}_- |E_0\rangle = s |E_0\rangle$ and the eigenvalue $s = -i\omega/\kappa + \mathcal{O}(1)$ (for a detailed derivation see Sec. A.3). The leading term in this eigenvalue is of order $\mathcal{O}(N)$ due to the rescaling $\omega = N\tilde{\omega}/2$, which accounts for the extensive nature of the Rabi frequency. Using this result the QFI reads

$$F(T,\varphi) = 4\frac{\omega^2}{\kappa}T, \tag{3.23}$$

in agreement with the results from the previous section.

In contrast, in the time crystal regime ($\omega \geq \omega_{\mathrm{c}}$), deriving an explicit expression for the stationary state is not practical and thus a different ansatz is made here. As can be seen in Fig. 3.3, the two-time correlations display a damped oscillating behavior and due to their time dependence they do not trivially cancel with the stationary intensity. Inspired by the ansatz in [39] for such two-time

correlations, a similar ansatz is chosen as

$$C_{S_+,S_-}^{S_-,S_+}(\tau) = \sum_{j=0}^{d} c_j e^{\lambda_j \tau}, \tag{3.24}$$

where the λ_j are eigenvalues of the physical Lindbladian $\mathcal{L}$ such that $\mathcal{L}[\rho_j] = \lambda_j \rho_j$ with the respective eigenstates ρ_j, and d is the number of eigenvalues. The Lindbladian is invariant under the transformation of Eq. (3.9) and thus the eigenvalues and eigenstates are independent of φ. The c_j are coefficients describing the decomposition of the time correlation in eigenmodes. A more detailed numerical analysis of the expansion in eigenmodes of the time correlation function is presented in Sec. A.2. The result of this analysis shows that the two-time correlations can be sufficiently described by the stationary and two additional non-stationary eigenmodes, such that
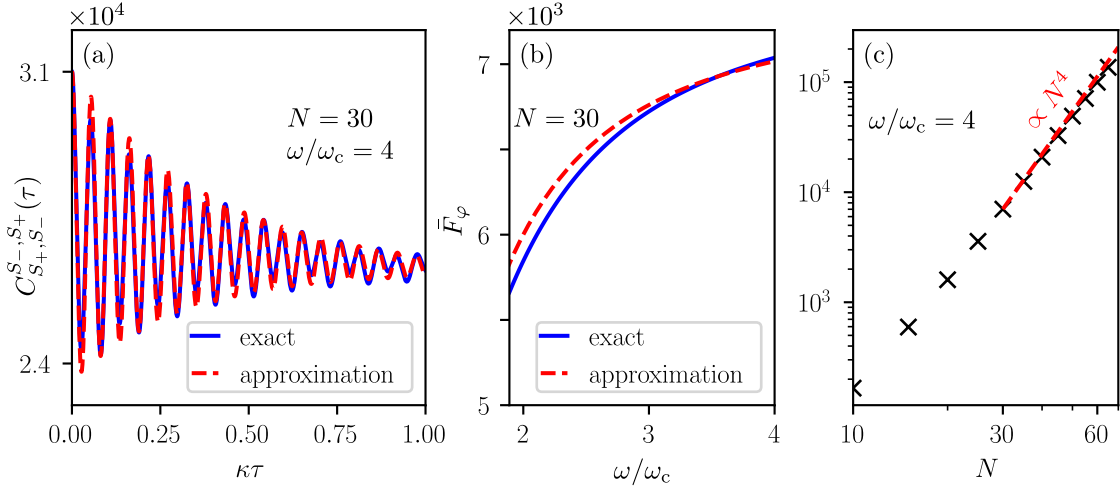
$$C_{S_+,S_-}^{S_-,S_+}(\tau) \approx c_0 + c_3^R e^{\lambda_3^R \tau} + c_3^C \left(e^{\lambda_3^C \tau} + e^{(\lambda_3^C)^* \tau} \right). \tag{3.25}$$

$\lambda_i^R = -\Gamma_i^R$, with $\Gamma_i^R \in \mathbb{R}^+$, are purely real eigenvalues and $\lambda_i^C = -\Gamma_i^C \pm \Omega_i$, with $\Gamma_i^C, \Omega_i \in \mathbb{R}^+$, are eigenvalues with non-vanishing imaginary part. The lower index orders the eigenvalues according to their real part in descending order. For the coefficients, one finds that

$$c_0 \approx \left| \langle \hat{S}_+ \hat{S}_- \rangle_{\rm ss} \right|^2, \ c_3^R \approx \frac{1}{4} \left[\langle \hat{S}_+^2 \hat{S}_-^2 \rangle_{\rm ss} - |\langle \hat{S}_+ \hat{S}_- \rangle_{\rm ss}|^2 \right] \text{ and } c_3^C \approx \frac{3 c_3^R}{2}. \tag{3.26}$$

As can be observed, the two-time correlation is an oscillating function enveloped by exponential decay. The time integrals in Eq. (3.22) can now be performed, such that

$$\lim_{T \to \infty} \frac{F(T,\varphi)}{T} = \bar{F}_\varphi \approx 4 \left\{ \kappa^2 \frac{\langle \hat{S}_+^2 \hat{S}_-^2 \rangle_{\rm ss} - \left| \langle \hat{S}_+ \hat{S}_- \rangle_{\rm ss} \right|^2}{2} \left(\frac{1}{\Gamma_3^R} + \frac{3\Gamma_3^C}{\Omega_3^2 + (\Gamma_3^C)^2} \right) + \kappa \langle \hat{S}_+ \hat{S}_- \rangle_{\rm ss} \right\}. \tag{3.27}$$

Figure 3.3: **Numerical results for the QFI in the MPS description.** (a) The two-time correlation function $C_{S_+,S_-}^{S_-,S_+}(\tau)$ as a function of the correlation time for $N = 30$ and $\omega/\omega_{\rm c} = 4$. Comparison of exact numerical simulation via propagation according to the Lindbladian (blue solid line) and approximation with two non-stationary eigenmodes (red dashed line). (b) Time rescaled QFI for fixed system size $N = 30$ as a function of the Rabi frequency ω. Comparison of exact numerical data from results of Sec. 3.3.1 (blue solid line) and data obtained using the approximated two-time correlations (red dashed line). (c) Time rescaled QFI in the time crystal regime computed according to Eq. (3.27) as a function of the system size N for $\omega/\omega_{\rm c} = 4$. A scaling of $\bar{F}_\varphi \propto N^\alpha$ with $\alpha = 3.876 \pm 0.008$ is obtained by a power law fit to the data. Deviations from the ideal N^4 scaling can occur due to the finite Rabi frequency ω used in the computations.

As predicted in Sec. 3.3.1, the expression Eq. (3.27) displays a linear asymptotic scaling in T. The intriguing difference to the stationary regime is that, due to the non-trivial two-time correlations, the QFI in the time crystal regime features a contribution $\propto \langle \hat{S}_+^2 \hat{S}_-^2 \rangle_{\mathrm{ss}} - |\langle \hat{S}_+ \hat{S}_- \rangle_{\mathrm{ss}}|^2$. In [43], this type of correlation is studied in more detail. First, they show that deep within the time crystal regime, the correlations have an asymptotic scaling in system size as N^4. This scaling comes at the expense of an increasing Rabi frequency $\omega = N\tilde{\omega}/2$, which is required to remain in the time crystal regime as the system size increases. Second, they find that the correlations saturate with increasing Rabi frequency ω in the same way as the QFI saturates, as shown in Fig. 3.2 and Fig. 3.3.

Indeed, as shown in Fig. 3.3, one recovers the results from Sec. 3.3.1 with numerical computations of the expectation values and eigenvalues in Eq. (3.27). Both the saturation with increasing Rabi frequency ω and the scaling with system size close to $\bar{F}_\varphi \propto N^4$ can be observed. Accordingly, the enhancement of the QFI in the time crystal regime can be attributed to collective effects beyond the collective emission of photons. These collective effects manifest in a non-trivial time dependence of the two-time intensity correlations and thus directly affect the emission field of the system.

4. Measurement protocols

In the previous chapters, the main properties of the BTC are presented (see Sec. 2.2), and its application to quantum sensing with respect to the estimation of an optical phase shift is discussed (see Sec. 3.3). An expression for the QFI in the time crystal regime is computed (see Eq. (3.27)), showing scaling beyond the Heisenberg limit in the system size and standard quantum scaling in the measurement time. This raises an immediate question: Is there a measurement protocol that saturates the QCRB?

The main challenge in finding a measurement protocol that saturates the QCRB is to define an appropriate measurement apparatus, that enables access to the quantum enhancement observed in the QFI. The search for such a protocol leads to the theory of cascaded quantum systems and dark states, which is explained in Sec. 4.1. A numerical approximation of the estimation error using a cascaded system protocol, which shows better-than-HL scaling in system size, is computed and it is shown analytically, that this measurement protocol is optimal in the stationary regime of the BTC. The results for the cascaded system protocol are then compared to a homodyne detection protocol in Sec. 4.2, revealing an advantage of the cascaded protocol in the time crystal regime.
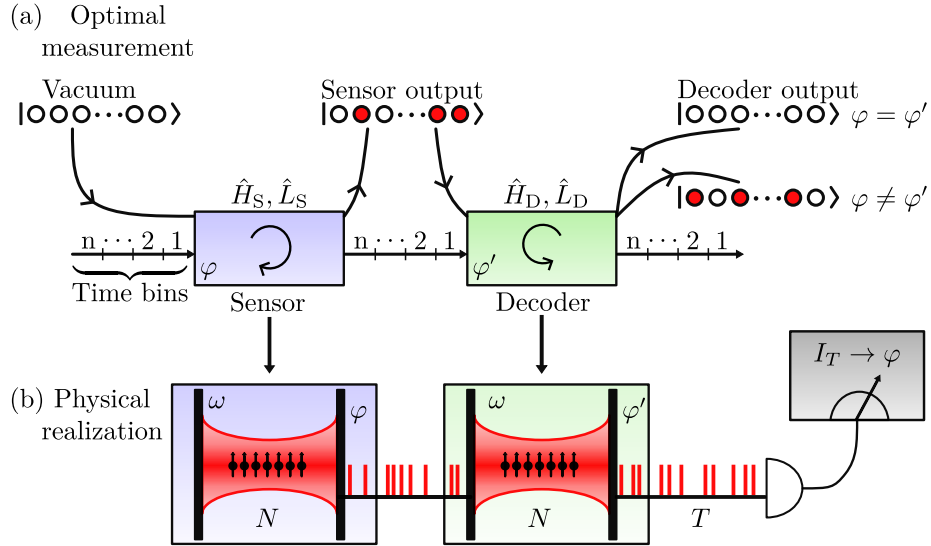
4.1. Cascaded System Protocol

Figure 4.1: **Cascaded sensor and decoder setup.** (a) An optimal measurement is constructed by guiding the sensor output to an engineered decoder. The time bin modes of the emission field interact sequentially with the sensor and the decoder. The decoder implements an optimal measurement of the sensor and its output in the vicinity of φ'. If the true value φ imprinted on the sensor output is in the vicinity of φ', the output of the cascaded system is dark and the decoder maps the sensor output back to the vacuum. (b) A possible physical realization of a sensor and decoder measurement setup for the estimation of an optical phase shift φ. Both sensor and decoder are identical BTCs, connected, for example, by a waveguide. The phase shift φ' imprinted on photons emitted by the decoder is tunable. The decoder output is monitored over a measurement time T. If the phase shifts coincide, such that $\varphi = \varphi'$, the decoder output is dark. Adapted from [38].

The notion of strong quantum correlations between the BTC and its emission field in the time crystal regime gives rise to a family of measurement protocols, where the emission field of the

system, containing the parameter φ, is monitored using an auxiliary quantum system. In such a situation, the system carrying the parameter φ can be thought of as a quantum sensor and the system attributed to the measurement apparatus as a decoder, retrieving the information about φ from the sensor output. In [46], the systematic construction of such measurement protocols, allowing for efficient unraveling of the information inscribed on the emission field of an open quantum system, is formulated. Essentially, an optimal measurement, saturating the QCRB, can be achieved by using an appropriate copy of the sensor as the decoder. Such an appropriate decoder has an interesting connection to dark states, since it can be constructed, such that it maps the emission field to its vacuum, as described in [79]. In [38], a cascaded quantum system protocol with a BTC, similar to the model in Sec. 2.2 as a sensor and decoder is used to estimate the Rabi frequency ω_{S} of the sensor. If the decoder Rabi frequency ω_{D} equals ω_{S}, this type of protocol saturates the QCRB in the stationary regime and has an advantage over simple photon counting in the time crystal regime. Motivated by these results, a similar measurement setup is used in this section in order to estimate the optical phase shift φ imprinted on the sensor output, as described in Sec. 3.3.

The cascaded system in Fig. 4.1 is described by the cascaded Hamiltonian $\hat{H}_{\text{casc}}$ and jump operator $\hat{L}_{\text{casc}}$ [79]

$$
\begin{aligned}
\hat{H}_{\text{casc}} &= \hat{H}_{\text{S}} + \hat{H}_{\text{D}} - \frac{i}{2}\left(\hat{L}_{\text{D}}^{\dagger}\hat{L}_{\text{S}} - \hat{L}_{\text{S}}^{\dagger}\hat{L}_{\text{D}}\right), \\
\hat{L}_{\text{casc}} &= \hat{L}_{\text{S}} + \hat{L}_{\text{D}}.
\end{aligned}
\tag{4.1}
$$

$\hat{H}_{\text{S}}$ ($\hat{H}_{\text{D}}$) is the Hamiltonian of the individual sensor (decoder) and $\hat{L}_{\text{S}}$ ($\hat{L}_{\text{D}}$) a respective jump operator describing the sensor (decoder). $\hat{H}_{\text{casc}}$ contains all coherent processes and $\hat{L}_{\text{casc}}$ describes the emission of a photon by the cascaded system, which can be observed in the decoder output. Monitoring of the decoder output over a measurement time T yields the time averaged intensity

$$
I_T = \frac{1}{T}\int_0^T dN(t),
\tag{4.2}
$$

where $dN(t)$ is a random variable with $dN(t) = 1$ if a photon is detected at time t and $dN(t) = 0$ otherwise. Its average value is $\mathbb{E}[dN(t)] = dt\,\text{Tr}\left[\hat{L}_{\text{casc}}^{\dagger}\hat{L}_{\text{casc}}\rho(t)\right]$, where $\mathbb{E}[\bullet]$ is the average over all possible emission trajectories, and ρ is the cascaded system density matrix [58]. The time averaged intensity can be described by large deviations theory [77, 80], showing that its long time limit approaches its mean value [58]

$$
\lim_{T\to\infty} I_T = \lim_{T\to\infty} \mathbb{E}[I_T] = \text{Tr}\left[\hat{L}_{\text{casc}}^{\dagger}\hat{L}_{\text{casc}}\rho_{\text{ss}}\right],
\tag{4.3}
$$

with the stationary state $\lim_{t\to\infty}\rho(t) = \rho_{\text{ss}}$ and the stationary intensity $\lim_{T\to\infty} I_T$. As the estimation of an optical phase shift imprinted on photons emitted by the sensor BTC is studied, its Hamiltonian and jump operator read

$$
\hat{H}_{\text{S}} = \omega\hat{S}_{\text{x}}^{\text{S}} \quad \text{and} \quad \hat{L}_{\text{S}} = \sqrt{\kappa}e^{-i\varphi}\hat{S}_{-}^{\text{S}}.
\tag{4.4}
$$

As a decoder, a BTC with identical system size N and Rabi frequency ω is proposed. On the photons emitted by that decoder BTC, a tunable phase shift φ' is imprinted, such that the decoder Hamiltonian and jump operator read

$$
\hat{H}_{\text{D}} = \omega\hat{S}_{\text{x}}^{\text{D}} \quad \text{and} \quad \hat{L}_{\text{D}} = \sqrt{\kappa}e^{-i\varphi'}\hat{S}_{-}^{\text{D}}.
\tag{4.5}
$$

Here, $\hat{S}_{\alpha}^{j} = \sum_{i=1}^{N}\sigma_{\alpha}^{i,j}/2$, with $\alpha \in \{\text{x}, \text{y}, \text{z}\}$, are again collective angular momentum operators with the Pauli matrices $\sigma_{\alpha}^{i,j}$. i denotes the index of an emitter in the sensor (decoder) for $j = \text{S}$ ($j = \text{D}$). In Sec. A.4, it is shown that this choice of the decoder emerges as the optimal decoder in the stationary regime, as proposed by [46]. For arbitrary values of φ and φ', the cascaded operators

thus read

$$\hat{H}_{\text{casc}}(\Delta\varphi) = \omega\left(\hat{S}_{\text{x}}^{\text{S}} + \hat{S}_{\text{x}}^{\text{D}}\right) - \frac{i\kappa}{2}\left(e^{-i\Delta\varphi}\hat{S}_{+}^{\text{D}}\hat{S}_{-}^{\text{S}} - e^{i\Delta\varphi}\hat{S}_{+}^{\text{S}}\hat{S}_{-}^{\text{D}}\right),$$

$$\hat{L}_{\text{casc}}(\Delta\varphi) = \sqrt{\kappa}\left(e^{-i\varphi}\hat{S}_{-}^{\text{S}} + e^{-i\varphi'}\hat{S}_{-}^{\text{D}}\right) = \sqrt{\kappa}e^{-i\varphi'}\left(e^{-i\Delta\varphi}\hat{S}_{-}^{\text{S}} + \hat{S}_{-}^{\text{D}}\right),$$

(4.6)

with the phase difference $\Delta\varphi = \varphi - \varphi'$. The global phase $e^{-i\varphi'}$ of the cascaded jump operator can be neglected, since the LME defining the dynamics of the cascaded system is invariant under changes of such global phase. For $\Delta\varphi = 0$, the stationary state generated by $\hat{H}_{\text{casc}}(0)$ and $\hat{L}_{\text{casc}}(0)$ is a pure dark state $\rho_{\text{ss}} = |D\rangle\langle D|$, satisfying the dark state conditions

$$(1)\ \hat{L}_{\text{casc}}|D\rangle = 0 \text{ and } (2)\ \hat{H}_{\text{casc}}|D\rangle = \epsilon|D\rangle.$$

(4.7)

Condition (1) ensures that no emission of photons occurs in the state $|D\rangle$ and condition (2) that the dark state does not evolve into a different state. The dark state can be interpreted as the vacuum of the coupled ladder operator $\hat{J}_{-} = \hat{S}_{-}^{\text{S}} + \hat{S}_{-}^{\text{D}} = \hat{L}_{\text{casc}}(0)\kappa^{-1/2}$. Its explicit form reads [38]

$$|D\rangle = \sum_{J=0}^{2S} A_J(\omega, \kappa)|J, -J\rangle,$$

(4.8)

where the states $|J, -J\rangle$ are states in the eigenbasis of the coupled angular momentum operator $\hat{J}_{\alpha} = \hat{S}_{\alpha}^{\text{S}} + \hat{S}_{\alpha}^{\text{D}}$, the coefficients A_J obey a simple recursion relation (see Sec. A.5), and $S = N/2$ is the angular momentum of the individual BTCs. Remarkably, this dark stationary state emerges for arbitrary values of ω/ω_{c}, as also seen in Fig. 4.2.
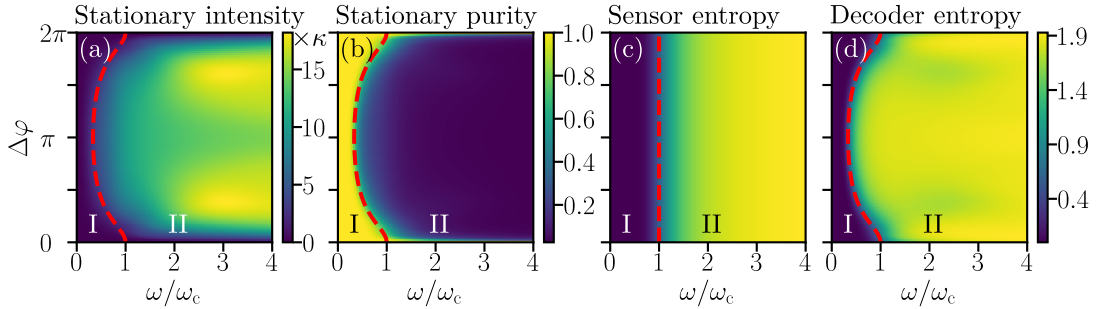

Figure 4.2: **Stationary properties of the cascaded system.** For (a)-(d), the system size is fixed to $N = 6$. (a) Stationary intensity, in units of κ, of the cascaded system for varying ω and $\Delta\varphi$. For $\Delta\varphi = 0 \mod 2\pi$, the output of the cascaded system is dark. (b) Purity of the stationary state. Close to the dark state condition $\Delta\varphi = 0$, the stationary state is pure. (c) Von Neumann entropy of the stationary state, reduced to the sensor. (d) Von Neumann entropy of the stationary state, reduced to the decoder. For (a), (b) and (d), the red dashed line corresponds to the mean-field transition line of the cascaded system from the stationary regime (I) to the cascaded time crystal regime (II). For (b), the red dashed line corresponds to the mean-field transition line of a single BTC from the stationary regime (I) to the time crystal regime (II).

Fig. 4.2 displays a phase transition of the cascaded system along the transition line $\omega_{\text{c,casc}}(\Delta\varphi) = \omega_{\text{c}}/\sqrt{5 - 4\cos(\Delta\varphi)}$, as computed in Sec. A.6. For $\Delta\varphi = 0$, this transition line equals the critical frequency of a single BTC and shifts towards lower values of ω for $\Delta\varphi \neq 0$. Below this transition line, the cascaded system is in a product state, with the sensor and decoder in a coherent state of the respective jump operators (see Sec. A.3). Effectively, both sensor and decoder are in the stationary regime individually below this transition line, resulting in a cascaded stationary regime. For $\omega > \omega_{\text{c,casc}}(\Delta\varphi)$, the decoder transitions to a time crystal regime resulting in a cascaded time crystal regime and for $\omega > \omega_{\text{c}}$, also the sensor transitions to a time crystal regime (see Fig. 4.3). Note, that the cascaded system transition line inherits the extensive nature of the critical driving $\omega_{\text{c}} = N\kappa/2$. This is accounted for by the rescaling $\omega = N\tilde{\omega}/2$ as in the single system.

The cascaded stationary regime is characterized by a low stationary intensity and a pure stationary state. The sensor and decoder are disentangled due to the product state nature of the

stationary state. In contrast, in the cascaded time crystal regime, only for $\Delta\varphi = 0$ the stationary intensity vanishes and the stationary state is pure. For $\Delta\varphi \neq 0$, the stationary intensity is high and the stationary state is mixed. For $\omega > \omega_c$, the sensor and decoder are highly entangled, as characterized by the von Neumann entropy $S(\rho_{\text{ss}}^i) = -\text{Tr}\left[\rho_{\text{ss}}^i \ln \rho_{\text{ss}}^i\right]$ of the stationary state reduced to both sensor ($i = \text{S}$) and decoder ($i = \text{D}$). It is close to its maximum for both sensor and decoder individually and especially for $\Delta\varphi = 0$ in the cascaded time crystal regime.
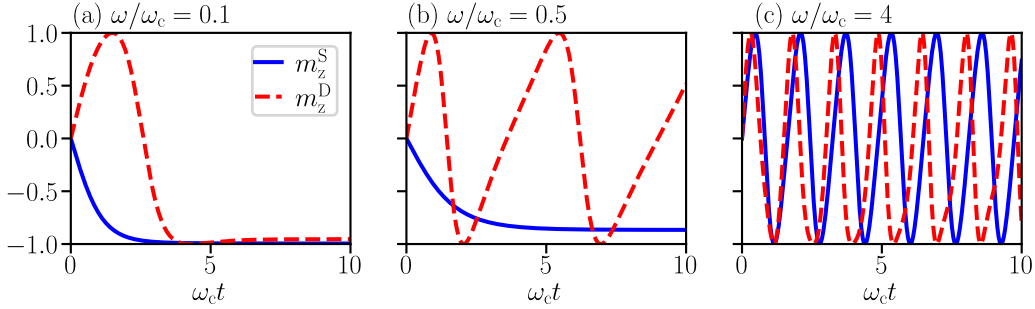

Figure 4.3: **Sensor and decoder mean field quantities along the phase diagram.** Mean-field expectation value $\lim_{N\to\infty} 2\langle\hat{S}_z^i\rangle/N = m_z^i$, with $i = \text{S}$ for the sensor (red dashed lines) and $i = \text{D}$ the decoder (blue solid line), for different positions in the phase diagram. $\omega_c = N\kappa/2$ is the critical frequency and both ω and t are measured in units of ω_c to obtain a well-defined limit. For all panels, $\Delta\varphi = \pi$. (a) $\omega/\omega_c = 0.1$, with sensor and decoder in the stationary regime. (b) $\omega/c = 0.5$, with the sensor in the stationary regime and the decoder displaying time crystal behavior. (c) $\omega/\omega_c = 4$, with both sensor and decoder in the time crystal regime.

The parameter φ is estimated from the monitored decoder output intensity I_T. This is achieved by counting the number M of emissions by the cascaded system and computing $I_T = M/T$ over a long measurement time $T \gg \kappa^{-1}$. The precision of this type of measurement can be described by the estimation error or error propagation formula [38]

$$\delta\varphi = \sqrt{\mathbb{E}\left[I_T^2\right] - \mathbb{E}\left[I_T\right]^2} \left|\frac{\partial\mathbb{E}[I_T]}{\partial\varphi}\right|^{-1}, \tag{4.9}$$

where the first term on the right-hand side is the standard deviation of the intensity I_T, and the second term describes the sensitivity of I_T to changes in φ. The estimation error is lower bounded by the QCRB as $\delta\varphi \geq 1/\sqrt{F(\varphi)}$ [38]. The statistics of the number of photon emissions M can be described by the generating function [77]

$$Z_{\text{count}}(s, \Delta\varphi) := \sum_{M=0}^{\infty} p_M(T, \Delta\varphi)e^{-sM}, \tag{4.10}$$

with the probability $p_M(T, \Delta\varphi)$ of observing M emissions until time T. In the long time limit, the generating function has the large deviation form $Z_{\text{count}}(s) \approx e^{T\theta(s, \Delta\varphi)}$ with the large deviation function $\theta(s, \Delta\varphi)$ [77]. Z_{count}, p_M and θ inherit a $\Delta\varphi$-dependence from Eq. (4.3) and the operators $\hat{L}_{\text{casc}}(\Delta\varphi)$. $\theta(s, \Delta\varphi)$ can be computed as the dominant eigenvalue of the tilted ME [38, 77, 80, 81]

$$\partial_t\rho_s = \mathcal{L}_{\text{casc}}[\rho_s] + (e^{-s} - 1)\hat{L}_{\text{casc}}(\Delta\varphi)\rho_s\hat{L}_{\text{casc}}^\dagger(\Delta\varphi), \tag{4.11}$$

with the physical Lindbladian $\mathcal{L}_{\text{casc}}$ of the cascaded system and a bias described by s. For $s = 0$, Eq. (4.11) generates the physical dynamics and for $s \neq 0$ it generates an ensemble of trajecotries with the bias e^{-sM} [77, 81]. The estimation error can thus be approximated in terms of the large deviations function $\theta(s, \Delta\varphi)$ as

$$\overline{\delta\varphi} := \sqrt{T}\delta\varphi \approx \frac{\sqrt{\partial_s^2\theta(s, \Delta\varphi)}}{|\partial_\varphi\partial_s\theta(s, \Delta\varphi)|}\Bigg|_{s=0} = \frac{\overline{\sigma_{I_T}}}{|\partial_\varphi I_T|}, \tag{4.12}$$

with the time rescaled standard deviation $\overline{\sigma_{I_T}} = \sqrt{\partial_s^2 \theta(s, \Delta\varphi)}|_{s=0}$, the time rescaled estimation error $\overline{\delta\varphi}$, and the derivative of the long time averaged intensity $-\partial_\varphi \partial_s \theta(s, \Delta\varphi)|_{s=0} = \partial_\varphi I_T$. It follows immediately that the estimation error decreases with measurement time as $\delta\varphi \propto 1/\sqrt{T}$, obeying the standard quantum limit for long measurement times.

In the stationary regime ($\omega < \omega_{c,casc}(\Delta\varphi)$), the dominant eigenvalue of Eq. (4.11) can be computed using a HP approach (see Sec. A.6), yielding

$$\theta(s, \Delta\varphi) = 2\frac{\omega^2}{\kappa}(e^{-s} - 1)(1 - \cos(\Delta\varphi)). \tag{4.13}$$

The resulting time rescaled estimation error reads

$$\overline{\delta\varphi} = \sqrt{\frac{\kappa(1 - \cos(\Delta\varphi))}{2\omega^2 \sin^2(\Delta\varphi)}}. \tag{4.14}$$

For $\Delta\varphi \to \pi$, this expression diverges and for $\Delta\varphi \to 0$, the estimation error reads $\overline{\delta\varphi} = \sqrt{\kappa}/(2\omega)$, saturating the QCRB. Also, Eq. (4.14) agrees with the numerical results in Fig. 4.4 if the estimation error is evaluated below the transition line $\omega_{c,casc}(\Delta\varphi)$. Note that, due to the rescaling $\omega = N\tilde{\omega}/2$, the expression in Eq. (4.14) effectively scales as N^{-1}, assuming that the Rabi frequency adjusted appropriately.
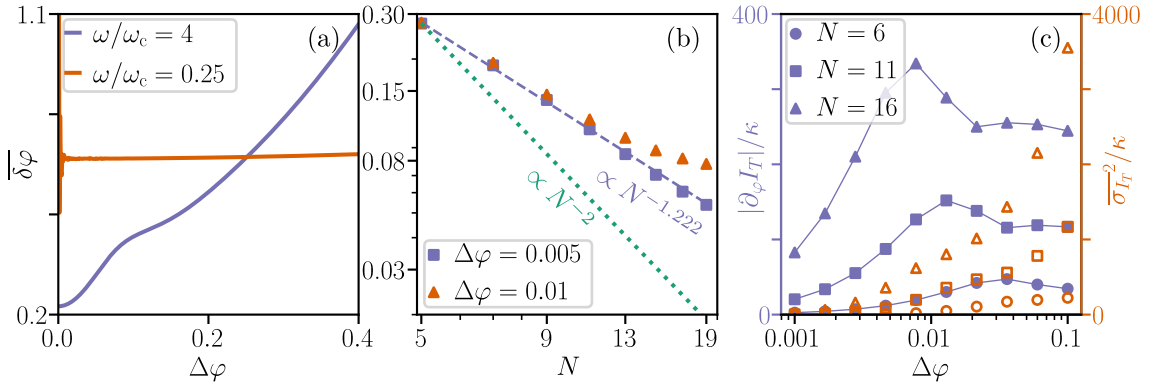

Figure 4.4: **Numerical results for the estimation error using a cascaded measurement protocol.** (a) Estimation error $\overline{\delta\varphi}$ using the cascaded measurement protocol for varying phase difference $\Delta\varphi$, evaluated at two different positions in the phase diagram. For $\omega/\omega_c = 0.25$, the numerical results show instabilities in the limiting case $\Delta\varphi \to 0$. In this panel, $N = 6$. (b) Estimation error $\overline{\delta\varphi}$ for varying system size N. The green dotted line indicates the limit for the estimation error predicted in Sec. 3.3.2. (c) Absolute derivative (left purple axis) and variance (right orange axis) of the intensity in the long time limit of the cascaded system, evaluated at $\omega/\omega_c = 4$ for different values of N. All results are obtained by diagonalization of Eq. (4.11).

In the time crystal regime ($\omega > \omega_{c,casc}(\Delta\varphi)$) and close to the dark state condition $\Delta\varphi = 0$, the estimation error is smaller than in the stationary regime. Remarkably, it also shows a scaling with system size stronger than the standard quantum and the Heisenberg limit (HL). One finds a scaling of $\overline{\delta\varphi} \propto N^{-\alpha}$ with $\alpha = 1.222 \pm 0.018$ for $\Delta\varphi = 0.005$, and $\alpha = 1.04 \pm 0.04$ for $\Delta\varphi = 0.01$. As for the QFI, this scaling of the estimation error is only realized if the Rabi frequency is increased according to the rescaling $\omega = N\tilde{\omega}/2$ as the system size N increases, ensuring that one remains in the time crystal regime.

For intermediate values of $\Delta\varphi$, the estimation error displays a plateau. As can be seen in panel (c) of Fig. 4.4, the derivative of the stationary intensity w.r.t. to φ has a N-dependent maximum that shifts closer to the dark state condition $\Delta\varphi = 0$ for increasing N. The maximum becomes more pronounced with increasing N. The variance $\overline{\sigma_{I_T}}$, on the other hand, increases monotonously w.r.t. φ and N. Both aspects lead to the observed plateau in the estimation error. Since both $\lim_{\Delta\varphi \to 0} \partial_\varphi I_T = 0$ and $\lim_{\Delta\varphi \to 0} \overline{\sigma_{I_T}} = 0$, numerical results can only be computed for finite $\Delta\varphi$.

4.2. Homodyne Detection Protocol

The cascaded measurement setup presented in the previous section shows quantum enhancement of the estimation precision, particularly in the time crystal regime. In order to highlight the advantage of the cascaded setup over other measurement setups in the long time limit, it is compared to a homodyne detection protocol in this section. This section is based on the results of [58, 64].

With the setup shown in Fig. 4.5, one can access information of the quadratures of the emission field by mixing it with the field of a strong local oscillator. Specifically, one can measure the homodyne current

$$J_\beta(t) = N\sqrt{\kappa}\,\langle \hat{m}_\beta(t)\rangle_{\mathrm{H}} + \frac{dW(t)}{dt}, \tag{4.15}$$

where $\hat{m}_\beta(t) = (\hat{S}_- e^{i(\beta-\varphi)} + \hat{S}_+ e^{-i(\beta-\varphi)})/N$ is a general rescaled quadrature and $W(t)$ a Wiener process. The subscript H indicates expectation values with respect to the conditioned state of the system in the homodyne detection protocol. The phase β is a tunable parameter depending on the chosen measurement setup. The Wiener process can be removed by averaging over small time intervals of $\Delta t \sim \kappa^{-1}$, or by taking the average over multiple measurements.
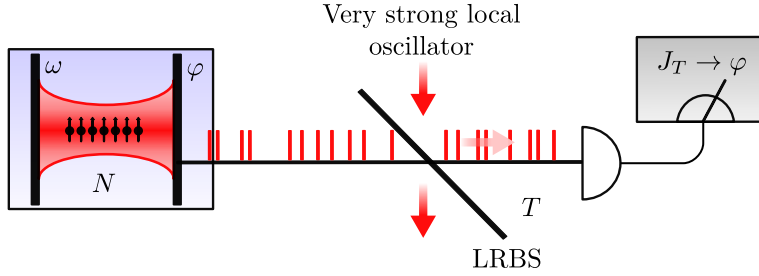

Figure 4.5: **Homodyne detection protocol** The output of a single BTC, including a phase shift φ imprinted on emitted photons, is superposed with the field of a strong local oscillator via a low reflectivity beam splitter (LRBS). The resulting time averaged homodyne current over the measurement time T is monitored. Adapted from [38].

The long time limit of the homodyne current does not vanish in general, but for the specific case $\varphi = \beta$, one finds $\lim_{t\to\infty}\langle\hat{m}_\beta(t)\rangle = \langle\hat{m}_{\mathrm{x}}\rangle_{\mathrm{ss}} = 0$. The moments of the time integrated homodyne current

$$K_T = \int_0^T J_\beta(t)dt, \tag{4.16}$$

can be determined via the generating function

$$Z_{\mathrm{hom}}(s,\varphi-\beta) = \int dK e^{-sK} p_K(T,\varphi-\beta), \tag{4.17}$$

where $p_K(T,\varphi-\beta) = P(K_T = K)$ is the probability of observing $K_T = K$. In the long time limit, this moment generating function has the large deviation form $Z(s) \approx e^{T\theta(s,\varphi-\beta)}$, with the large deviation function $\theta(s,\varphi-\beta)$. Z_{hom}, p_K and θ inherit a $\varphi-\beta$ dependence from J_β. The large deviation function θ can be computed as the eigenvalue with largest real part of the deformed ME

$$\partial_t\rho_s = \mathcal{L}[\rho] - s\sqrt{\kappa}\left(\hat{S}_- e^{i(\beta-\varphi)}\rho + \rho\hat{S}_+ e^{-i(\beta-\varphi)}\right) + \frac{s^2}{2}\rho, \tag{4.18}$$

with the physical Lindbladian of a single BTC $\mathcal{L}$. For $s \to 0$, the physical LME is recovered. The time averaged homodyne current is defined as $J_T := \mathbb{E}[K_T]/T$. Due to the large deviations structure, J_T approaches a constant value in the long time limit $\lim_{T\to\infty} J_T = -\partial_s\theta(s,\varphi-\beta)$ and

its variance behaves as $\lim_{T\to\infty} \mathbb{E}[J_T^2] - \mathbb{E}[J_T]^2 = \lim_{T\to\infty} \partial_s^2 \theta(s, \varphi - \beta)/T$. The estimation error for measuring φ via monitoring of the long time averaged homodyne current reads

$$\delta\varphi = \sqrt{\mathbb{E}[J_T^2] - \mathbb{E}[J_T]^2} \left| \frac{\partial \mathbb{E}[J_T]}{\partial \varphi} \right|^{-1}, \tag{4.19}$$

which is lower bounded by the QCRB as $\delta\varphi \geq 1/\sqrt{F(\varphi)}$. With the large deviation function $\theta(s, \varphi - \beta)$, this can be approximated by

$$\overline{\delta\varphi} := \sqrt{T}\delta\varphi \approx \left. \frac{\sqrt{\partial_s^2 \theta(s, \varphi - \beta)}}{|\partial_\varphi \partial_s \theta(s, \varphi - \beta)|} \right|_{s=0} = \left. \frac{\overline{\sigma_{J_T}}}{|\partial_\varphi J_T|} \right|_{s=0}, \tag{4.20}$$

with the time rescaled standard deviation $\overline{\sigma_{J_T}} := \sqrt{\partial_s^2 \theta(s, \varphi - \beta)}|_{s=0}$, the time rescaled estimation error $\overline{\delta\varphi}$ and the derivative of the homodyne current in the long time limit $\partial_\varphi J_T := -\partial_\varphi \partial_s \theta(s, \varphi - \beta)|_{s=0}$. Similar to the estimation error in the cascaded measurement protocol, the estimation error decreases with measurement time as $\delta\varphi \propto 1/\sqrt{T}$, obeying the standard quantum limit for long measurement times.
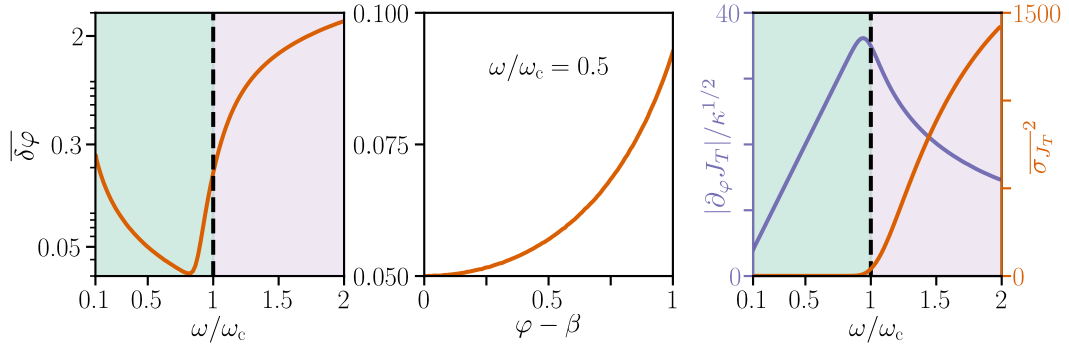

Figure 4.6: **Numerical results for the estimation error using homodyne detection.** Results presented are all for $N = 40$. (a) Estimation error for the parameter φ for varying Rabi frequency ω. For (a) and (c), the black dashed line indicates the phase transition of a single BTC at $\omega = \omega_{\rm c}$. (b) Estimation error for φ for varying homodyne phase difference $\varphi - \alpha$, evaluated within the stationary regime at $\omega/\omega_{\rm c} = 0.5$. (c) Absolute derivative w.r.t. φ and variance of the time averaged homodyne current J_T for varying Rabi frequency ω.

In the stationary regime ($\omega < \omega_{\rm c}$), the large deviation function $\theta(s, \varphi - \beta)$ can be computed using a HP approach (see Sec. A.3) as

$$\theta(s, \varphi - \beta) = -2s\frac{\omega}{\sqrt{\kappa}} \sin(\varphi - \beta) + \frac{s^2}{2}. \tag{4.21}$$

The resulting time rescaled estimation error reads

$$\overline{\delta\varphi} = \frac{\sqrt{\kappa}}{2\omega|\cos(\varphi - \beta)|}. \tag{4.22}$$

The estimation error is minimal if $\varphi - \beta = 0 \mod \pi$, where steps of π cause a sign change in the homodyne current. At the minimum condition, the estimation error saturates the QCRB. This approximation agrees with the numerical results in Fig. 4.6 deep within the stationary regime. Assuming that the Rabi frequency ω is increased with the system size according to the rescaling $\omega = N\tilde{\omega}/2$, this yields a scaling of the estimation error with system size as $\overline{\delta\varphi} \propto N^{-1}$.

In the vicinity of the critical frequency $\omega_{\rm c}$ and in the area of the time crystal regime ($\omega > \omega_{\rm c}$) shown in Fig. 4.6, the estimation error increases with the Rabi frequency ω. This has a twofold reason: On the one hand, the homodyne current becomes less sensitive to changes in the phase φ.

On the other hand, the homodyne current's variance increases with ω in the time crystal regime, whereas it remains constant in the stationary regime. This shows that the homodyne measurement protocol has the same estimation error as the cascaded measurement protocol in the stationary regime. However, in the time crystal regime, the cascaded measurement protocol has an advantage over homodyne detection in the long time limit and can (at least partly) exploit the advantage of the time crystal regime as predicted by the QFI.

5. Conclusion and Outlook

In this thesis, the application of a BTC as a resource for quantum enhanced estimation of an optical phase shift was investigated. First, the properties of the BTC were studied, using a LME description of its time evolution. This highlighted the emergence of collective nonequilibrium behavior and two distinct phases, the stationary regime and the time crystal regime. The thermodynamic limit allowed to clearly separate these phases at a critical driving, with a time translation invariant stationary state below the critical driving and persistent temporal oscillations of the system observables above the critical driving. The critical driving displayed a linear dependence on the system size, shifting towards larger values with increasing system size. In addition to the LME description of open quantum systems, the MPS representation of the global system and environment state was introduced, capturing both the system evolution and the emission field of the BTC.

Following this study, it was shown, that the BTC can be used for measuring an optical phase shift φ. By imprinting such a phase shift on and monitoring the emission field of a BTC, the BTC showed to be a resource for quantum enhanced sensing. In order to quantify the fundamental bounds of such measurement, the formalism of (quantum) parameter estimation was employed. The MPS representation showed to be a powerful tool to derive a convenient expression for the QFI in terms of the dominant eigenvalue of a deformed ME. Numerical results revealed an advantage of the QFI in the time crystal regime over the stationary regime. In addition, it was shown that the QFI can be expressed in terms of the two-time and single-time intensity correlations. Investigation of these correlations revealed vanishing two-time correlations in the stationary regime and damped-oscillatory two-time correlations in the time crystal regime. As a result, the QFI showed a N^4 scaling with system size N in the time crystal regime, in comparison to N^2 in the stationary regime. Due to the linear dependence of the critical driving on the system size, this scaling behavior was only achieved when the driving was appropriately increased as system size increased.

In order to harness the BTC as a resource for quantum enhanced sensing, two different measurement protocols were analyzed. First, a cascaded system protocol featuring an auxiliary BTC, used as a decoder for the emission field of the sensor, was employed. In this protocol, monitoring of the cascaded system output using an ideal photoncounter was assumed. A tunable phase shift φ' was imprinted on the decoder output and for $\varphi = \varphi'$, a pure dark state emerged, leading to a dark output of the cascaded system. Second, a homodyne detection protocol was studied, where the homodyne current from the sensor was monitored. It was shown both numerically and analytically, that the estimation error for both protocols saturates the QCRB in the stationary regime. Analytical results were obtained using a HP approach. In the time crystal regime, the estimation error for the cascaded system protocol showed an advantage over the stationary regime, scaling with $N^{-1.222}$, and thus surpassing the HL. In contrast, the estimation error for the homodyne detection protocol was higher in the time crystal regime than in the stationary regime. As for the QFI, achieving this scaling behavior required increased driving as system size increased.

The results of this work thus can be summarized as follows: On the one hand, the fundamental bound for the estimation precision of an optical phase shift using a BTC was determined by computing the QFI. The QFI showed scaling with system size above the HL in the time crystal regime. On the other hand, it was shwon, that a cascaded system protocol can be implemented to achieve a scaling of the estimation error better than the HL. However, the investigations did not show, whether or not the cascaded system protocol achieves saturation of the QCRB in the time crystal regime. The enhancement of the QFI and the estimation error in the time crystal regime came at the expense of increased driving as system size increased, due to a linear dependence of the critical driving on the system size.

Further study should thus investigate and compare the performance of different measurement

protocols and how the strong system size scaling of the QFI in the time crystal regime can be harnessed. On the one hand, this could involve further analysis of the cascaded system protocol in the time crystal regime similar to [46]. On the other hand, it should be noted, that the protocols employed in this work infer the parameter φ by monitoring the time averaged intensity and homodyne current. Going beyond such time averaged quantities leaves room for further studies.

One way to achieve this is to analyze the full FI for a given measurement protocol. In [40, 51], a path to saturate the QFI for a class of measurement protocols such as ideal photoncounting or homodyne detection is shown. A similar approach could be applied to the homodyne detection protocol employed in this work, in order to determine the FI in that case.

In addition to that, the notion of two-time correlations in the QFI allows for further investigation. Such time correlations can be exploited for measurement protocols, for example, by measuring them using interferometers [39]. Also, sensing applications with other quantum systems displaying non-vanishing temporal correlations should be studied [82]. Interesting time-dependence of the QFI can emerge on intermediate time scales when accounting for criticality and phase transitions [45, 47], which could as well be analyzed for the setup presented in this work.

As a conclusion, the application of open quantum systems as quantum sensors shows the potential for increased precision in the presence of collective nonequilibrium behavior. In order to develop new types of sensor designs, both theoretical and experimental boundaries will need to be pushed in order to determine practical realizations of such quantum sensors in realistic environments.

Bibliography

[1]   J. A. Needham, I. Lesanovsky, and B. Olmos, "Subradiance-protected excitation transport", New J. Phys. **21**, 073061 (2019).

[2]   R. H. Dicke, "Coherence in spontaneous radiation processes", Phys. Rev. **93**, 99–110 (1954).

[3]   K. Sacha and J. Zakrzewski, "Time crystals: a review", Rep. Prog. Phys. **81**, 016401 (2017).

[4]   D. V. Else, C. Monroe, C. Nayak, and N. Y. Yao, "Discrete time crystals", Annu. Rev. Condens. Matter Phys. **11**, 467–499 (2020).

[5]   M. P. Zaletel, M. Lukin, C. Monroe, C. Nayak, F. Wilczek, and N. Y. Yao, "Colloquium: quantum and classical discrete time crystals", Rev. Mod. Phys. **95**, 031001 (2023).

[6]   D. V. Else, B. Bauer, and C. Nayak, "Floquet time crystals", Phys. Rev. Lett. **117**, 090402 (2016).

[7]   V. Khemani, A. Lazarides, R. Moessner, and S. L. Sondhi, "Phase structure of driven quantum systems", Phys. Rev. Lett. **116**, 250401 (2016).

[8]   Z. Gong, R. Hamazaki, and M. Ueda, "Discrete time-crystalline order in cavity and circuit qed systems", Phys. Rev. Lett. **120**, 040404 (2018).

[9]   N. Y. Yao, A. C. Potter, I.-D. Potirniche, and A. Vishwanath, "Discrete time crystals: rigidity, criticality, and realizations", Phys. Rev. Lett. **118**, 030401 (2017).

[10] R. R. W. Wang, B. Xing, G. G. Carlo, and D. Poletti, "Period doubling in period-one steady states", Phys. Rev. E **97**, 020202 (2018).

[11] F. M. Gambetta, F. Carollo, M. Marcuzzi, J. P. Garrahan, and I. Lesanovsky, "Discrete time crystals in the absence of manifest symmetries or disorder in open quantum systems", Phys. Rev. Lett. **122**, 015701 (2019).

[12] A. Lazarides, S. Roy, F. Piazza, and R. Moessner, "Time crystallinity in dissipative floquet systems", Phys. Rev. Res. **2**, 022002 (2020).

[13] A. Riera-Campeny, M. Moreno-Cardoner, and A. Sanpera, "Time crystallinity in open quantum systems", Quantum **4**, 270 (2020).

[14] B. Zhu, J. Marino, N. Y. Yao, M. D. Lukin, and E. A. Demler, "Dicke time crystals in driven-dissipative quantum many-body systems", New J. Phys. **21**, 073028 (2019).

[15] K. Chinzei and T. N. Ikeda, "Time crystals protected by floquet dynamical symmetry in hubbard models", Phys. Rev. Lett. **125**, 060601 (2020).

[16] H. Keßler, P. Kongkhambut, C. Georges, L. Mathey, J. G. Cosme, and A. Hemmerich, "Observation of a dissipative time crystal", Phys. Rev. Lett. **127**, 043602 (2021).

[17] R. J. L. Tuquero, J. Skulte, L. Mathey, and J. G. Cosme, "Dissipative time crystal in an atom-cavity system: influence of trap and competing interactions", Phys. Rev. A **105**, 043311 (2022).

[18] S. Sarkar and Y. Dubi, "Signatures of discrete time-crystallinity in transport through an open fermionic chain", Commun. Phys. **5**, 155 (2022).

[19] A. Cabot, F. Carollo, and I. Lesanovsky, "Metastable discrete time-crystal resonances in a dissipative central spin system", Phys. Rev. B **106**, 134311 (2022).

[20] F. Iemini, A. Russomanno, J. Keeling, M. Schirò, M. Dalmonte, and R. Fazio, "Boundary time crystals", Phys. Rev. Lett. **121**, 035301 (2018).

[21] F. Carollo and I. Lesanovsky, "Exact solution of a boundary time-crystal phase transition: time-translation symmetry breaking and non-markovian dynamics of correlations", Phys. Rev. A **105**, L040202 (2022).

[22] K. Tucker, B. Zhu, R. J. Lewis-Swan, J. Marino, F. Jimenez, J. G. Restrepo, and A. M. Rey, "Shattered time: can a dissipative time crystal survive many-body correlations?", New J. Phys. **20**, 123003 (2018).

[23] G. Buonaiuto, F. Carollo, B. Olmos, and I. Lesanovsky, "Dynamical phases and quantum correlations in an emitter-waveguide system with feedback", Phys. Rev. Lett. **127**, 133601 (2021).

[24] C. Lledó and M. H. Szymańska, "A dissipative time crystal with or without z2 symmetry breaking", New J. Phys. **22**, 075002 (2020).

[25] K. Seibold, R. Rota, and V. Savona, "Dissipative time crystal in an asymmetric nonlinear photonic dimer", Phys. Rev. A **101**, 033839 (2020).

[26] B. Bu ča and D. Jaksch, "Dissipation induced nonstationarity in a quantum gas", Phys. Rev. Lett. **123**, 260401 (2019).

[27] B. Bu ča, J. Tindall, and D. Jaksch, "Non-stationary coherent quantum many-body dynamics through dissipation", Nat. Commun. **10**, 1730 (2019).

[28] C. Booker, B. Buča, and D. Jaksch, "Non-stationarity and dissipative time crystals: spectral properties and finite-size effects", New J. Phys. **22**, 085007 (2020).

[29] L. F. d. Prazeres, L. d. S. Souza, and F. Iemini, "Boundary time crystals in collective *d*-level systems", Phys. Rev. B **103**, 184308 (2021).

[30] G. Piccitto, M. Wauters, F. Nori, and N. Shammah, "Symmetries and conserved quantities of boundary time crystals in generalized spin models", Phys. Rev. B **104**, 014307 (2021).

[31] A. C. Louren ço, L. F. d. Prazeres, T. O. Maciel, F. Iemini, and E. I. Duzzioni, "Genuine multipartite correlations in a boundary time crystal", Phys. Rev. B **105**, 134422 (2022).

[32] M. Hajdu šek, P. Solanki, R. Fazio, and S. Vinjanampathy, "Seeding crystallization in time", Phys. Rev. Lett. **128**, 080603 (2022).

[33] M. Krishna, P. Solanki, M. Hajdu šek, and S. Vinjanampathy, "Measurement-induced continuous time crystals", Phys. Rev. Lett. **130**, 150401 (2023).

[34] R. Mattes, I. Lesanovsky, and F. Carollo, "Entangled time-crystal phase in an open quantum light-matter system", Phys. Rev. A **108**, 062216 (2023).

[35] J. A. Muniz, D. Barberena, R. J. Lewis-Swan, D. J. Young, J. R. K. Cline, A. M. Rey, and J. K. Thompson, "Exploring dynamical phase transitions with cold atoms in an optical cavity", Nature **580**, 602–607 (2020).

[36] M. A. Norcia, M. N. Winchester, J. R. K. Cline, and J. K. Thompson, "Superradiance on the millihertz linewidth strontium clock transition", Sci. Adv. **2**, e1601231 (2016).

[37] G. Ferioli, A. Glicenstein, I. Ferrier-Barbut, and A. Browaeys, "A non-equilibrium superradiant phase transition in free space", Nat. Phys. **19**, 1345–1349 (2023).

[38] A. Cabot, F. Carollo, and I. Lesanovsky, "Continuous sensing and parameter estimation with the boundary time crystal", Phys. Rev. Lett. **132**, 050801 (2024).

[39] A. Cabot, F. Carollo, and I. Lesanovsky, "Quantum enhanced parameter estimation with monitored quantum nonequilibrium systems using inefficient photo detection", arXiv:2503.21753 [quant-ph] (2025).

[40] R. Mattes, A. Cabot, F. Carollo, and I. Lesanovsky, "Designing open spin-boson models for enabling quantum enhanced sensing through classical measurements", arXiv:2505.08756 [quant-ph] (2025).

[41] D. Braun, G. Adesso, F. Benatti, R. Floreanini, U. Marzolino, M. W. Mitchell, and S. Pirandola, "Quantum-enhanced measurements without entanglement", Rev. Mod. Phys. **90**, 035006 (2018).

[42] C. L. Degen, F. Reinhard, and P. Cappellaro, "Quantum sensing", Rev. Mod. Phys. **89**, 035002 (2017).

[43] H. J. Carmichael, "Analytical and numerical results for the steady state in cooperative resonance fluorescence", J. Phys. B: Atom. Mol. Phys. **13**, 3551 (1980).

[44] S. Gammelmark and K. Mølmer, "Fisher information and the quantum cramér-rao sensitivity limit of continuous measurements", Phys. Rev. Lett. **112**, 170401 (2014).

[45] T. Ilias, D. Yang, S. F. Huelga, and M. B. Plenio, "Criticality-enhanced quantum sensing via continuous measurement", PRX Quantum **3**, 010354 (2022).

[46] D. Yang, S. F. Huelga, and M. B. Plenio, "Efficient information retrieval for sensing via continuous measurement", Phys. Rev. X **13**, 031012 (2023).

[47] K. Macieszczak, M. ă. Gu ţ ă, I. Lesanovsky, and J. P. Garrahan, "Dynamical phase transitions as a resource for quantum enhanced metrology", Phys. Rev. A **93**, 022103 (2016).

[48] J. Gambetta and H. M. Wiseman, "State and dynamical parameter estimation for open quantum systems", Phys. Rev. A **64**, 042105 (2001).

[49] A. H. Kiilerich and K. Mølmer, "Estimation of atomic interaction parameters by photon counting", Phys. Rev. A **89**, 052110 (2014).

[50] F. Albarelli, M. A. C. Rossi, M. G. A. Paris, and M. G. Genoni, "Ultimate limits for quantum magnetometry via time-continuous measurements", New J. Phys. **19**, 123011 (2017).

[51] F. Albarelli, M. A. C. Rossi, D. Tamascelli, and M. G. Genoni, "Restoring Heisenberg scaling in noisy quantum metrology by monitoring the environment", Quantum **2**, 110 (2018).

[52] A. Shankar, G. P. Greve, B. Wu, J. K. Thompson, and M. Holland, "Continuous real-time tracking of a quantum phase below the standard quantum limit", Phys. Rev. Lett. **122**, 233602 (2019).

[53] F. Albarelli, M. A. C. Rossi, and M. G. Genoni, "Quantum frequency estimation with conditional states of continuously monitored independent dephasing channels", Int. J. Quantum. Inform. **18**, 1941013 (2020).

[54] M. A. C. Rossi, F. Albarelli, D. Tamascelli, and M. G. Genoni, "Noisy quantum metrology enhanced by continuous nondemolition measurement", Phys. Rev. Lett. **125**, 200505 (2020).

[55] H. I. Nurdin and M. Guţă, "Parameter estimation and system identification for continuously-observed quantum systems", Annu. Rev. Control **54**, 295–304 (2022).

[56] A. Godley and M. Guta, "Adaptive measurement filter: efficient strategy for optimal estimation of quantum Markov chains", Quantum **7**, 973 (2023).

[57] H. Cramér, "Mathematical methods of statistics" (Princeton University Press, Princeton, 1946).

[58] H. M. Wiseman and G. J. Milburn, "Quantum measurement and control" (Cambridge University Press, Cambridge, 2009).

[59] G. Lindblad, "On the generators of quantum dynamical semigroups", Commun. Math. Phys. **48**, 119–130 (1976).

[60] V. Gorini, A. Frigerio, M. Verri, A. Kossakowski, and E. Sudarshan, "Properties of quantum markovian master equations", Rep. Math. Phys. **13**, 149–173 (1978).

[61] G. S. Agarwal, A. C. Brown, L. M. Narducci, and G. Vetri, "Collective atomic effects in resonance fluorescence", Phys. Rev. A **15**, 1613–1624 (1977).

[62] L. M. Narducci, D. H. Feng, R. Gilmore, and G. S. Agarwal, "Transient and steady-state behavior of collective atomic systems driven by a classical field", Phys. Rev. A **18**, 1571–1576 (1978).

[63] D. Roberts and A. A. Clerk, "Exact solution of the infinite-range dissipative transverse-field ising model", Phys. Rev. Lett. **131**, 190403 (2023).

[64] A. Cabot, L. S. Muhle, F. Carollo, and I. Lesanovsky, "Quantum trajectories of dissipative time crystals", Phys. Rev. A **108**, L041303 (2023).

[65] V. Link, K. Luoma, and W. T. Strunz, "Revealing the nature of nonequilibrium phase transitions with quantum trajectories", Phys. Rev. A **99**, 062120 (2019).

[66] R. Puri and S. Lawande, "Exact steady-state density operator for a collective atomic system in an external field", Physics Letters A **72**, 200–202 (1979).

[67] F. Benatti, F. Carollo, R. Floreanini, and H. Narnhofer, "Quantum spin chain dissipative mean-field dynamics", J. Phys. A: Math. Theor. **51**, 325001 (2018).

[68] O. E. Lanford and D. Ruelle, "Observables at infinity and states with short range correlations in statistical mechanics", Commun. Math. Phys. **13**, 194–215 (1969).

[69] I. Lesanovsky, M. van Horssen, M. ă. Guţă, and J. P. Garrahan, "Characterization of dynamical phase transitions in quantum jump trajectories beyond the properties of the stationary state", Phys. Rev. Lett. **110**, 150401 (2013).

[70] F. Ciccarello, S. Lorenzo, V. Giovannetti, and G. M. Palma, "Quantum collision models: open system dynamics from repeated interactions", Phys. Rep. **954**, 1–70 (2022).

[71] F. Verstraete and J. I. Cirac, "Continuous matrix product states for quantum fields", Phys. Rev. Lett. **104**, 190405 (2010).

[72] J. Haegeman, J. I. Cirac, T. J. Osborne, and F. Verstraete, "Calculus of continuous matrix product states", Phys. Rev. B **88**, 085118 (2013).

[73] J. Liu, H. Yuan, X.-M. Lu, and X. Wang, "Quantum fisher information matrix and multiparameter estimation", J. Phys. A: Math. Theor. **53**, 023001 (2019).

[74] S. L. Braunstein and C. M. Caves, "Statistical distance and the geometry of quantum states", Phys. Rev. Lett. **72**, 3439–3443 (1994).

[75] L. Pezzè, M. A. Ciampini, N. Spagnolo, P. C. Humphreys, A. Datta, I. A. Walmsley, M. Barbieri, F. Sciarrino, and A. Smerzi, "Optimal measurements for simultaneous quantum estimation of multiple phases", Phys. Rev. Lett. **119**, 130504 (2017).

[76] L. Pezzè and A. Smerzi, "Quantum Theory of Phase Estimation", in *Proceedings of the International School of Physics "Enrico Fermi"*, Vol. 188 (IOS Press, Amsterdam, 2014).

[77] J. P. Garrahan and I. Lesanovsky, "Thermodynamics of quantum jump trajectories", Phys. Rev. Lett. **104**, 160601 (2010).

[78] J. Hannukainen and J. Larson, "Dissipation-driven quantum phase transitions and symmetry breaking", Phys. Rev. A **98**, 042113 (2018).

[79] K. Stannigel, P. Rabl, and P. Zoller, "Driven-dissipative preparation of entangled states in cascaded quantum-optical networks", New J. Phys. **14**, 063014 (2012).

[80] F. Carollo, J. P. Garrahan, I. Lesanovsky, and C. Pérez-Espigares, "Making rare events typical in markovian open quantum systems", Phys. Rev. A **98**, 010103 (2018).

[81] P. Zoller, M. Marte, and D. F. Walls, "Quantum jumps in atomic systems", Phys. Rev. A **35**, 198–207 (1987).

[82] G. Lee, R. Belyansky, L. Jiang, and A. A. Clerk, "Timescales, squeezing and heisenberg scalings in many-body continuous sensing", arXiv:2505.04591 [quant-ph] (2025).

A. Supplemental Material

A.1. Inner products for the QFI

The inner product $\langle\psi_\varphi|\psi'_\varphi\rangle$, evaluated at time T, reads

$$
\begin{aligned}
\langle\psi_\varphi(T)|\psi'_\varphi(T)\rangle &= \sum_{i_1,\ldots,i_n=0}^{1}\sum_{j=1}^{n} \langle\chi| K_{i_1}^\dagger \ldots K_{i_n}^\dagger K_{i_n} \ldots (\partial_\varphi K_{i_j}) \ldots K_{i_1} |\chi\rangle \\
&= \sum_{j=1}^{n} \mathrm{Tr}\left[\rho_{\mathrm{S}}(t_{j-1})K_{i_j}^\dagger \underbrace{\left(\sum_{i_{j+1},\ldots,i_n=0}^{1} K_{i_{j+1}}^\dagger \ldots K_{i_{j+1}}\right)}_{1}(\partial_\varphi K_{i_j})\right] \\
&= \sum_{j=1}^{n} \mathrm{Tr}\left[\rho_{\mathrm{S}}(t_{j-1})(-i\kappa\delta t)\hat{S}_+\hat{S}_-\right] \xrightarrow{\delta t\to 0} \kappa\int_0^T dt\, \mathrm{Tr}\left[\rho_{\mathrm{S}}(t)\hat{S}_+\hat{S}_-\right],
\end{aligned}
\tag{A.1}
$$

with the initial state of the system $|\chi_{\mathrm{S}}(0)\rangle = |\chi\rangle$. In a similar way, one can also determine the inner product $\langle\psi'_\varphi|\psi'_\varphi\rangle$

$$
\langle\psi'_\varphi(T)|\psi'_\varphi(T)\rangle = \sum_{j,k=1}^{n}\sum_{i_1,\ldots,i_n=0}^{1} \mathrm{Tr}\left[|\chi\rangle\langle\chi| K_{i_1}^\dagger \ldots (\partial_\varphi K_{i_k}^\dagger) \ldots K_{i_n}^\dagger K_{i_n} \ldots (\partial_\varphi K_{i_j}) \ldots K_{i_1}\right]. \tag{A.2}
$$

The appearing sums over j and k can be split into three sums, with $j=k$, $j>k$ and $j<k$. For $j=k$, one obtains

$$
\begin{aligned}
&\sum_{j=k=1}^{n}\sum_{i_1,\ldots,i_n=0}^{1} \mathrm{Tr}\left[|\chi\rangle\langle\chi| K_{i_1}^\dagger \ldots (\partial_\varphi K_{i_k}^\dagger) \ldots K_{i_n}^\dagger K_{i_n} \ldots (\partial_\varphi K_{i_j}) \ldots K_{i_1}\right] \\
&= \sum_{j=1}^{n}\sum_{i_{j+1},\ldots,i_n=0}^{1} \mathrm{Tr}\left[\rho_{\mathrm{S}}(t_{j-1})(\partial_\varphi K_{i_j}^\dagger) \ldots K_{i_n}^\dagger K_{i_n} \ldots (\partial_\varphi K_{i_j})\right] \\
&= \sum_{j=1}^{n} \mathrm{Tr}\left[\rho_{\mathrm{S}}(t_{j-1})\kappa\delta t\hat{S}_+\hat{S}_-\right] \xrightarrow{\delta t\to 0} \kappa\int_0^T dt\, \mathrm{Tr}\left[\rho_{\mathrm{S}}(t)\hat{S}_+\hat{S}_-\right].
\end{aligned}
\tag{A.3}
$$

And for the case $j>k$

$$
\begin{aligned}
&\sum_{j>k}\sum_{i_1,\ldots,i_n=0}^{1} \mathrm{Tr}\left[|\chi\rangle\langle\chi| K_{i_1}^\dagger \ldots (\partial K_{i_k}^\dagger) \ldots K_{i_n}^\dagger K_{i_n} \ldots (\partial_\varphi K_{i_j}) \ldots K_{i_1}\right] \\
&= \sum_{j>k}\sum_{i_{k+1},\ldots,i_n=0}^{1} \mathrm{Tr}\left[\rho_{\mathrm{S}}(t_{k-1})(\partial_\varphi K_{i_k}^\dagger) \ldots K_{i_n}^\dagger K_{i_n} \ldots (\partial_\varphi K_{i_j}) \ldots K_{i_k}\right] \\
&= \sum_{j>k}\sum_{i_{k+1},\ldots,i_n=0}^{1} \mathrm{Tr}\left[K_{i_j}^\dagger \ldots K_{i_n}^\dagger K_{i_n} \ldots (\partial_\varphi K_{i_j})(K_{i_{j-1}} \ldots K_{i_k}\rho_{\mathrm{S}}(t_{k-1})(\partial_\varphi K_{i_k}^\dagger) \ldots K_{i_{j-1}}^\dagger)\right] \\
&= \sum_{j>k} \mathrm{Tr}\left[(\kappa^2\delta t^2)\hat{S}_+\hat{S}_-(\hat{S}_-\rho_{\mathrm{S}}(t_{k-1})\hat{S}_+)(t_{j-1}-t_{k+1})\right] \\
&\xrightarrow{\delta t\to 0} \kappa^2\int_0^T dt \int_0^{T-t} d\tau\, \mathrm{Tr}\left[\hat{S}_+\hat{S}_- e^{\mathcal{L}\tau}(\hat{S}_-\rho_{\mathrm{S}}(t)\hat{S}_+)\right],
\end{aligned}
\tag{A.4}
$$

where $t_{j-1} - t_{k+1} =: \tau$ and the time evolution of $\mathcal{O}_1 \rho(t) \mathcal{O}_2$ from time t to time τ is written as $(\mathcal{O}_1 \rho(t) \mathcal{O}_2)(\tau) \xrightarrow{\delta t \to 0} e^{\tau \mathcal{L}} (\mathcal{O}_1 \rho(t) \mathcal{O}_2)$ [39]. The remaining sum for $k > j$ is the complex conjugate of the sum for $j > k$ and thus adds the same contribution since the result is real.

A.2. Approximate description of time correlations in the single system

In this section, the approximation of the two time correlations presented in Sec. 3.3.2 is benchmarked with exact results from evolution according to the LME and the relevant decay rates $\Gamma_3^{R/C}$ and the frequency Ω_3 are numerically computed. One observes, that the approximation via two dominant eigenmodes of the Lindbladian captures the overall dynamics of the two time correlations, while contributions by additional modes are present (see Fig. A.1). The used decay rates display only minor N-dependence in the analyzed range and similarly the rescaled frequency Ω_3/N, showing that the main dependence of the QFI on the system size can be attributed to the factor $\langle \hat{S}_+^2 \hat{S}_-^2 \rangle_{\text{ss}} - |\langle \hat{S}_+ \hat{S}_- \rangle_{\text{ss}}|^2$, which behaves as N^4 for $N \gg 1$ [43].
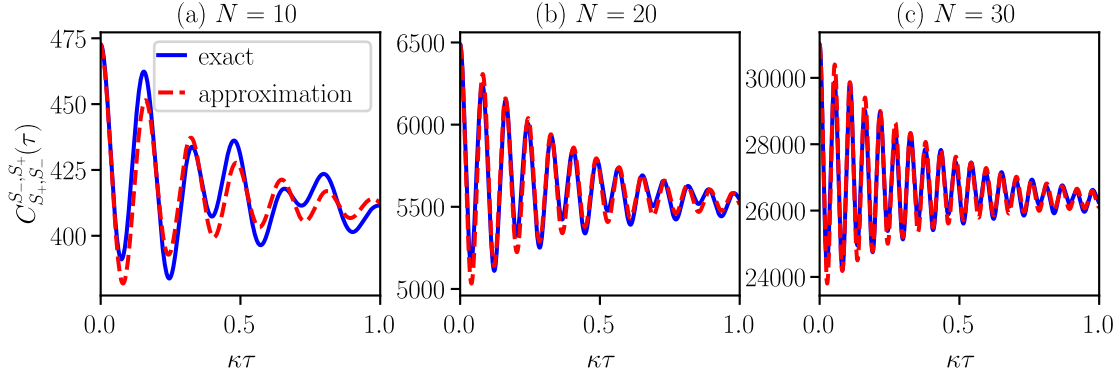

Figure A.1: **Benchmark for approximation of two-time intensity correlations in the time crystal regime.** Two time correlations $C_{S_+,S_-}^{S_-,S_+}(\tau)$, evaluated in the time crystal regime for $\omega/\omega_c = 4$. Comparison of data simulated via evolution according to the Lindbladian (blue solid line) and approximation via two dominant eigenmodes and the stationary eigenmode as in Sec. 3.3.2 (red dashed line), for varying system sizes with (a) $N = 10$, (b) $N = 20$, (c) $N = 30$.
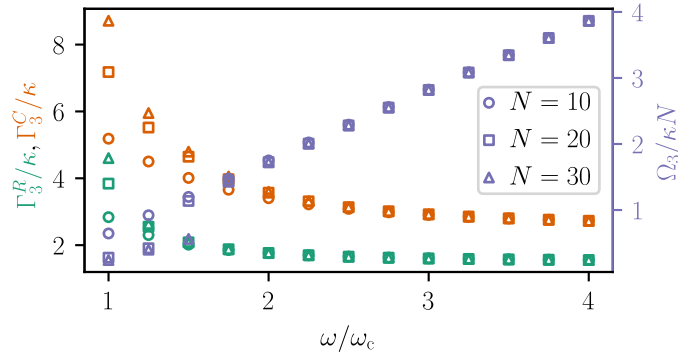

Figure A.2: **Numerical analysis of selected eigenmodes of the BTC.** Decay rates Γ_3^R and Γ_3^C and system rescaled frequency Ω_3/N, as used in the approximate description of two time correlations in Sec. 3.3.2, for varying Rabi frequency and for different system sizes. One can see, that deep within the time crystal regime, the rates $\Gamma_3^{R/C}$ saturate and the frequency Ω_3 increases with the Rabi frequency ω and system size. Deep within the time crystal regime, the rates do not show a N-dependence in the evaluated range of system sizes.

A.3. Holstein Prikmakoff approach to the single system

In this section, the application of the Holstein-Primakoff transformation to the individual sensor system is discussed as in [38]. This approach allows for a useful approximation in the stationary regime of the sensor system. The Holstein-Primakoff transformation is applied to the spin operators of the sensor system and expresses them in terms of bosonic ladder operators

$$\hat{S}_+ = \hat{b}^\dagger \sqrt{2S - \hat{b}^\dagger \hat{b}}, \ \ \hat{S}_- = \sqrt{2S - \hat{b}^\dagger \hat{b}} \hat{b}, \tag{A.5}$$

with $S = N/2$ as stated in Sec. 2.2. In the stationary regime, the bosonic mode described by the operators $\hat{b}^{(\dagger)}$ is assumed to be in a large displaced state, such that only quantum fluctuations around this large displaced state are studied

$$\hat{b} \to \hat{b} + \sqrt{S}\beta, \tag{A.6}$$

where β is a complex field, which is determined below. If S describes a large displacement, then $\epsilon = \frac{1}{\sqrt{S}}$ is a small parameter. The spin operators can be expanded in powers of ϵ as

$$\hat{m}_\alpha = \frac{\hat{S}_\alpha}{S} = \sum_{l=0}^\infty \epsilon^l \hat{m}_{\alpha,l}. \tag{A.7}$$

Explicit expressions up to order $\mathcal{O}(\epsilon)$ are given by

$$m_{+,0} = \sqrt{k}\beta^* \text{ and } \hat{m}_{+,1} = \frac{1}{2\sqrt{k}}[(4 - 3|\beta|^2)\hat{b}^\dagger - \beta^{*2}\hat{b}], \tag{A.8}$$

where $k = 2 - |\beta|^2$. The expanded operators are introduced in the LME, in order to determine the field β. However, it is helpful to account for the physical behaviour of the system before. It is known, that the critical point, at which the transition from the stationary regime to the time crystal phase occur,s scales with the system size as $\omega_c = N\kappa/2 = S\kappa$. This extensive character of the Rabi frequency can be accounted for by rescaling according to

$$\omega = \tilde{\omega}S, \ \ \tau = St, \tag{A.9}$$

where also the time scale of the dynamics is rescaled. With the rescaled operators and parameters, one obtains the LME

$$\partial_\tau \rho = -i\tilde{\omega}S[\hat{m}_\mathrm{x}, \rho] + \kappa S\left(\hat{m}_-\rho\hat{m}_+ - \frac{1}{2}\{\hat{m}_+\hat{m}_-, \rho\}\right). \tag{A.10}$$

In order to determine the field β, also the density matrix is expanded as

$$\rho = \sum_{l=0}^\infty \epsilon^l \rho_l. \tag{A.11}$$

In order to obtain the stationary state, the right-hand side of A.10 has to vanish. Up to $\mathcal{O}(\epsilon)$, this yields

$$0 = -i\tilde{\omega} \pm \kappa m_{\pm,0} \Rightarrow \beta\sqrt{2 - |\beta|^2} = -i\frac{\tilde{\omega}}{\kappa}, \tag{A.12}$$

from which β can be determined to $\beta = -i\sqrt{1 - \sqrt{1 - (\tilde{\omega}\kappa)^2}}$, which is only valid in the regime where $\tilde{\omega} \leq \kappa$, i.e. the stationary regime. For the dominant order of the rescaled ladder operators, one obtains

$$m_{\pm,0} = \pm\frac{i\tilde{\omega}}{\kappa}. \tag{A.13}$$

The term of $\mathcal{O}(1)$ of the LME yields

$$\partial_\tau \rho_0 = \kappa \left(\hat{m}_{-,1} \rho_0 \hat{m}_{+,1} - \frac{1}{2} \{ \hat{m}_{+,1} \hat{m}_{-,1}, \rho_0 \} \right). \tag{A.14}$$

In order to obtain the stationary state, one can make the ansatz

$$\rho_{0,\mathrm{ss}} = |E_0\rangle \langle E_0|, \tag{A.15}$$

where the state $|E_0\rangle$ is annihilated by the fluctuation of the lowering operator $\hat{m}_{-,1}$. By expanding $\hat{m}_{-,1} = A\hat{b} + B\hat{b}^\dagger$ with the coefficients

$$A = \frac{1 + 3\sqrt{1 - (\tilde{\omega}/\kappa)^2}}{2\sqrt{1 + \sqrt{1 - (\tilde{\omega}/\kappa)^2}}}, \ B = \frac{1 - \sqrt{1 - (\tilde{\omega}/\kappa)^2}}{2\sqrt{1 + \sqrt{1 - (\tilde{\omega}\kappa)^1}}}, \tag{A.16}$$

one can eventually determine the stationary state to

$$|E_0\rangle = \frac{1}{\sqrt{\mathcal{N}}} |0\rangle + \frac{1}{\sqrt{\mathcal{N}}} \sum_{n=1}^{\infty} (-1)^n \left(\frac{B}{A} \right)^n \sqrt{\frac{(2n-1)!!}{2n!!}} |2n\rangle. \tag{A.17}$$

$\mathcal{N}$ is a normalization constant, $|n\rangle$ is a Fock state in the bosonic mode and one has to note, that this is only well defined for $|B/A| \le 1$ and in the stationary regime $\tilde{\omega} < \kappa$.

Calculation of the QFI

In order to determine an expression for the QFI, one needs to analyze the tilted ME

$$\partial_t \rho = -i\omega[\hat{S}_\mathrm{x}, \rho] + \kappa \hat{S}_- \rho \hat{S}_+ - \frac{\kappa}{2} \{ \hat{S}_+ \hat{S}_-, \rho \} + \left(e^{-i\Delta\varphi} - 1 \right) \kappa \hat{S}_- \rho \hat{S}_+. \tag{A.18}$$

Plugging in the rescaled operators and parameters yields the rescaled deformed ME

$$\partial_\tau \rho = -i\tilde{\omega} S[\hat{m}_\mathrm{x}, \rho] + \kappa S \hat{m}_- \rho \hat{m}_+ - S\frac{\kappa}{2} \{ \hat{m}_+ \hat{m}_-, \rho \} + \left(e^{-i\Delta\varphi} - 1 \right) \kappa S \hat{m}_- \rho \hat{m}_+. \tag{A.19}$$

Here one can make an ansatz for the dominant eigenstate similar to the undeformed ME as

$$\rho_0 = |E_0^{\varphi_1}\rangle \langle E_0^{\varphi_2}|. \tag{A.20}$$

$|E_0^\varphi\rangle$ denotes the stationary state of the fluctuations Eq. (A.17) evaluated at the point φ. As this state is independent of φ, one could neglect the index, but it is carried here in order to keep the notation consistent with situations, where this is not the case. The action of $\hat{m}_-$ can be expanded as follows

$$\hat{m}_- |E_0^{\varphi_1}\rangle = \left(m_{-,0}^{\varphi_1} + \frac{1}{\sqrt{S}} \hat{m}_{-,1}^{\varphi_1} + ... \right) |E_0^{\varphi_1}\rangle \ \text{and} \ \langle E_0^{\varphi_2}| \hat{m}_- = \langle E_0^{\varphi_2}| \left(m_{-,0}^{\varphi_2} + \frac{1}{\sqrt{S}} \hat{m}_{-,1}^{\varphi_2} + ... \right). \tag{A.21}$$

With this ansatz, the deformed ME yields

$$\partial_\tau \rho_0 = \mathcal{L}[\rho_0] + \left(e^{-i\Delta\varphi} - 1 \right) \kappa S \left(m_{-,0}^{\varphi_1} + \frac{1}{\sqrt{S}} \hat{m}_{-,1}^{\varphi_1} + ... \right) |E_0^{\varphi_1}\rangle \langle E_0^{\varphi_2}| \left(m_{-,0}^{\varphi_2} + \frac{1}{\sqrt{S}} \hat{m}_{-,1}^{\varphi_2} + ... \right), \tag{A.22}$$

with $\Delta\varphi := \varphi_1 - \varphi_2$ and $m_{\pm,0}^\varphi = m_{\pm,0} = \pm i\tilde{\omega}/\kappa$ as before. Of interest are the derivatives w.r.t. φ of the dominant eigenvalue of this tilted ME. The contribution $\mathcal{L}[\rho_0]$ vanishes due to $\hat{m}_{-,1}^\varphi |E_0^\varphi\rangle = 0$ and thus one is interested in the second term in the deformed ME. The leading term of $\mathcal{O}(S)$ reads

$$\left(e^{-i\Delta\varphi} - 1 \right) \kappa S m_{-,0}^{\varphi_1} m_{+,0}^{\varphi_2} |E_0^{\varphi_1}\rangle \langle E_0^{\varphi_2}| = \left(e^{-i\Delta\varphi} - 1 \right) \kappa S \frac{\tilde{\omega}^2}{\kappa^2} \rho_0 = \underbrace{\left(e^{-i\Delta\varphi} - 1 \right) S \frac{\tilde{\omega}^2}{\kappa} \rho_0}_{=:\tilde{\lambda}_0(\varphi_1, \varphi_2)}. \tag{A.23}$$

The next-to-dominant term of order $\mathcal{O}(\sqrt{S})$ vanishes, because $\hat{m}^{\varphi}_{-,1}|E^{\varphi}_0\rangle = 0$. Thus one finds for the dominant eigenvalue of the deformed ME up to $\mathcal{O}(\epsilon)$

$$\lambda_0(\Delta\varphi) = S\tilde{\lambda}_0(\Delta\varphi), \tag{A.24}$$

where the factor of S comes from the previous rescaling. This expression is benchmarked with results from diagonalization of Eq. (3.15). This yields a compact expression for the QFI in the stationary regime

$$\lim_{T\to\infty} \frac{F(\varphi,T)}{T} = 4\partial_{\varphi_1}\partial_{\varphi_2}\operatorname{Re}(\lambda_{\mathrm{E}})\big|_{\varphi_1=\varphi_2} = 4\partial_{\varphi_1}\partial_{\varphi_2}\operatorname{Re}\left(e^{-i(\varphi_1-\varphi_2)}-1\right)\frac{S^2\tilde{\omega}^2}{\kappa}\big|_{\varphi_1=\varphi_2} \tag{A.25}$$

$$= 4\cos(\varphi_1-\varphi_2)\frac{S^2\tilde{\omega}^2}{\kappa}\big|_{\varphi_1=\varphi_2} \tag{A.26}$$

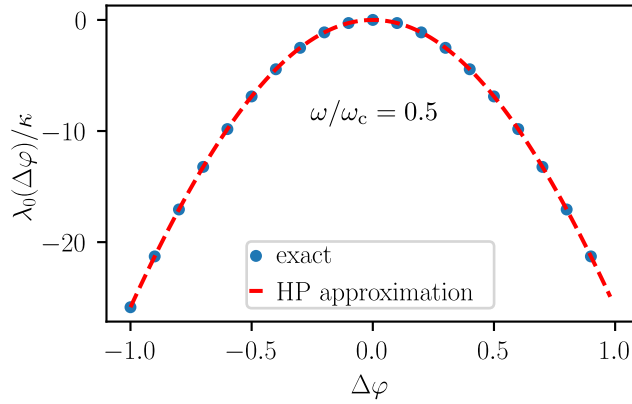$$= 4\frac{\omega^2}{\kappa}. \tag{A.27}$$

Figure A.3: **Benchmark for the approximate expression of the QFI.** Dominant eigenvalue λ_0 of the deformed ME Eq. (3.15) for varying $\Delta\varphi = \varphi_1 - \varphi_2$, fixed system size $N = 30$ and in the stationary regime $\omega/\omega_{\mathrm{c}} = 0.5$. Comparison of data obtained using the HP approach (red dashed line) and diagonalization of Eq. (3.15) (blue dots).

Estimation error for homodyne detection

Similarly to the approximation of the QFI in the stationary regime, one can also approximate the estimation error of the parameter φ via homodyne detection. In the stationary regime, the respective deformed ME Eq. (4.18) is rescaled according to

$$\omega = S\tilde{\omega}, \ \tau = St, \ \hat{m}_\alpha = \frac{\hat{S}_\alpha}{S} = \sum_{l=0}^{\infty}\epsilon^l\hat{m}_{\alpha,l}, \ \epsilon = \frac{1}{\sqrt{S}} = \sqrt{\frac{2}{N}}. \tag{A.28}$$

With these rescaled quantities, Eq. (4.18) reads

$$\partial_\tau\rho = -i\tilde{\omega}S[\hat{m}_{\mathrm{x}},\rho] + \kappa S\hat{m}_-\rho\hat{m}_+ - S\frac{\kappa}{2}\{\hat{m}_+\hat{m}_-,\rho\}$$
$$+ s\sqrt{\kappa}\left(\hat{m}_-e^{i(\alpha-\varphi)}\rho + \rho\hat{m}_+e^{-i(\alpha-\varphi)}\right) + \frac{s^2}{2}\frac{\rho}{S}. \tag{A.29}$$

One can make an ansatz for the dominant eigenstate here as $\rho_0 = |E_0\rangle\langle E_0|$. By plugging in to the rescaled deformed ME, one obtains

$$\partial_\tau\rho_0 \approx s\sqrt{\kappa}\left\{e^{i(\beta-\varphi)}(m_{-,0}+\hat{m}_{-,1}+\dots)\rho_0 + \rho_0(m_{+,0}+\hat{m}_{+,1}+\dots)e^{-i(\varphi-\beta)}\right\} + \frac{s^2}{2}\frac{\rho_0}{S}. \tag{A.30}$$

Using the self-consistency relations for $m_{\pm,0}$, the contribution to the dominant eigenvalue up to order $\mathcal{O}(1)$ is

$$s\sqrt{\kappa}\frac{i\tilde{\omega}}{\kappa}\left(e^{-i(\beta-\varphi)} - e^{i(\beta-\varphi)}\right) = 2s\frac{\tilde{\omega}}{\sqrt{\kappa}}\sin(\beta-\varphi). \tag{A.31}$$

Since the variance of the homodyne current is given by the second derivative $\partial_s^2\theta(s)$, one also has to include corrections of higher orders of ϵ. The correction of $\mathcal{O}(\epsilon)$ vanishes and the correction of $\mathcal{O}(\epsilon^2)$ reads $s^2/2S$, such that the dominant eigenvalue of the rescaled deformed ME reads

$$\tilde{\theta}(s,\varphi-\beta) = 2s\frac{\omega}{S\sqrt{\kappa}}\sin(\beta-\varphi) + \frac{s^2}{2S} \tag{A.32}$$

which is related to the dominant eigenvalue of Eq. (4.18) via $\theta(s,\varphi-\beta) = S\tilde{\theta}(s,\varphi-\beta)$. For the estimation error, this means

$$\left(\overline{\delta\varphi}\right)^2 = \frac{\partial_{\tilde{s}^2}\theta(\tilde{s},\varphi-\beta)}{(\partial_\varphi\partial_{\tilde{s}}\theta(\tilde{s},\varphi-\beta))^2}\bigg|_{\tilde{s}=0} = \frac{1}{(2\frac{\omega}{\sqrt{\kappa}}\cos(\beta-\varphi))^2} = \frac{\kappa}{4\omega^2\cos^2(\beta-\varphi)}. \tag{A.33}$$

This result is numerically benchmarked with results from diagonalization of Eq. (4.18) as shown in Fig. A.4.
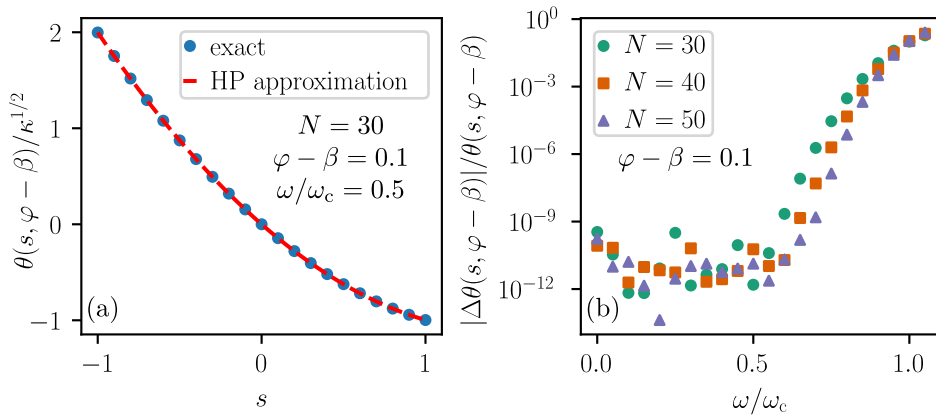

Figure A.4: **Benchmark for the approximate expression of the homodyne estimation error.** (a) Dominant eigenvalue of Eq. (4.18) as a function of the bias parameter s for $\varphi - \beta = 0.1$, fixed system size $N = 30$ and in the stationary regime $\omega/\omega_c = 0.5$. The red dashed line is obtained evaluating the result obtained by the HP approach, whereas the blue dots are computed by diagonalization of Eq. (4.18). (b) Relative error of the dominant eigenvalue θ as a function of the Rabi frequency ω, for different system sizes and fixed values $\varphi - \beta = 0.1$ and $s = -0.05$. The error is defined as the absolute difference of the HP approximated value and the and the exact diagonalized value and both divided by the exact value. One observes that the error increases towards the critical Rabi frequency, but is small in a large portion of the stationary regime.

A.4. Construction of the optimal decoder in the stationary regime

This section follows the construction of an optimal decoder of [46], applies it to the case presented in Sec. 4.1 and shows that the decoder used there is optimal, at least in the stationary regime of the BTC.

The measurement of the decoder output can be interpreted as recording the trajectory of emissions $\{i_1, \ldots, i_n\}$ in time bins of size δt over a measurement time $T = n\delta t$. It is assumed, that the time bins δt are small enough, that at maximum one photon is emitted per time bin, meaning

that $i_j \in \{0, 1\}$. This interpretation of the measurement procedure implies a Matrix Product description. Monitoring of the decoder output implements the measurement

$$\Pi^{\mathrm{DE}}_{\{i_j\}} = U^\dagger_{\mathrm{DE}}(T)\Pi_{\{i_j\}}U_{\mathrm{DE}}(T), \tag{A.34}$$

acting on the decoder and emission field state $\rho_{\mathrm{D}}(0) \otimes \rho_{\mathrm{E}}(T)$ before their interaction. $\rho_{\mathrm{D}}(0) = |\chi_{\mathrm{D}}(0)\rangle \langle\chi_{\mathrm{D}}(0)|$ is the decoder initial state and $\rho_{\mathrm{E}}(T)$ describes the emission field at time T, after the interaction with the sensor. It is $\rho_{\mathrm{E}}(T)$ from which the information about the parameter φ shall be extracted. $\Pi_{\{i_j\}} = \bigotimes^n_{j=1} |i_j\rangle \langle i_j|$ is the projector on the observed trajectory in the basis of the sensor and decoder emission field time bin modes, interacting sequentially with the sensor and decoder [70]. U_{DE} is a unitary, describing the joint evolution of the decoder and emission field. In the MPS description of the decoder and emission field state, this unitary is a Matrix Product Operator. The resulting measurement $\Pi^{\mathrm{DE}}_{\{i_j\}}$ thus also has a Matrix Product structure.

The global sensor and emission field state is a pure MPS $|\psi_\varphi(T)\rangle$, with the true value of the optical phase shift φ. Any projective measurement $\{\Pi^{\mathrm{SE}}_k\}$ of the state $|\psi_\varphi(T)\rangle$ containing the projector

$$\Pi^{\mathrm{SE}}_0 = |\psi_{\varphi'}(T)\rangle \langle\psi_{\varphi'}(T)|, \tag{A.35}$$

is optimal [73–76] in the vicinity of φ', in the sense that it saturates the QCRB evaluated at φ'. This also means that if the parameter φ' is tuned to the true value φ, then the projective measurement $\{\Pi^{\mathrm{SE}}_k\}$ is optimal for the true realization of φ. To allow for an optimal measurement, the effective measurement of the decoder emission field $\Pi^{\mathrm{DE}}_{\{i_j\}}$ has to obey the same emission field structure as Π^{SE}_0 for at least one specific trajectory $\{m_j\}$. This condition can be formulated as

$$U_{\mathrm{DE}}(\varphi', T)\left[\Pi^{\mathrm{SE}}_0 \otimes \rho_D(0)\right]U^\dagger_{\mathrm{DE}}(\varphi', T) = \Pi_{\{m_j\}} \otimes \rho_{\mathrm{SD}}(\varphi', T). \tag{A.36}$$

Physically, this means that the time evolution $U_{\mathrm{DE}}(\varphi', T)$ transforms the sensor and emission field state Π^{SE}_0, in the case that $\varphi = \varphi'$, into the specific trajectory $\{m_j\}$ of the emission field as described by the projector $\Pi_{\{m_j\}}$. In this transformation the sensor and decoder evolve into a general state $\rho_{\mathrm{SD}}(\varphi', T)$, that is discarded. U_{DE} and ρ_{SD} inherit a dependence on φ' from Eq. (A.35). The elegance of Eq. (A.36) is, that the trajectory $\{m_j\}$ can be chosen as desired. A convenient choice is the vacuum $\{m_j\} = \{0, 0, \ldots, 0\}$, which describes a dark decoder output.

A general construction of a decoder satisfying Eq. (A.36) can be challenging. However, in the long time limit, a convenient construction can be found, if the sensor evolves according to a time-homogeneous LME with support for a stationary state $\rho_{\mathrm{S,ss}} = \sum^d_{k=1} p_{k,\mathrm{ss}}(\varphi') |k_{\mathrm{ss}}(\varphi')\rangle_{\mathrm{S}\,\mathrm{S}}\langle k_{\mathrm{ss}}(\varphi')|$. In such case, the Hamiltonian and jump operator of the decoder should be chosen as

$$\hat{H}_{\mathrm{D}}(\varphi') = -\frac{1}{2}\sum_{k,k'}\sqrt{\frac{p_{k',\mathrm{ss}}(\varphi')}{p_{k,\mathrm{ss}}(\varphi')}}\left[{}_{\mathrm{S}}\langle k_{\mathrm{ss}}(\varphi')|\hat{H}_{\mathrm{S,NH}}(\varphi')|k'_{\mathrm{ss}}(\varphi')\rangle_{\mathrm{S}} \times |\tilde{k}'_{\mathrm{ss}}(\varphi')\rangle_{\mathrm{D}\,\mathrm{D}}\langle\tilde{k}_{\mathrm{ss}}(\varphi')| + \mathrm{h.c.}\right] \tag{A.37}$$

$$\hat{L}_{\mathrm{D}}(\varphi') = -\sum_{k,k'}\sqrt{\frac{p_{k',\mathrm{ss}}(\varphi')}{p_{k,\mathrm{ss}}(\varphi')}}\,{}_{\mathrm{S}}\langle k_{\mathrm{ss}}(\varphi')|\hat{J}_{\mathrm{S}}(\varphi')|k'_{\mathrm{ss}}(\varphi')\rangle_{\mathrm{S}} \times |\tilde{k}'_{\mathrm{ss}}(\varphi')\rangle_{\mathrm{D}\,\mathrm{D}}\langle\tilde{k}_{\mathrm{ss}}(\varphi')|, \tag{A.38}$$

where $\hat{H}_{\mathrm{S,NH}} := \hat{H}_{\mathrm{S}} - i\hat{L}^\dagger_{\mathrm{S}}\hat{L}_{\mathrm{S}}/2$ is an effective non-Hermitian Hamiltonian of the sensor and $|\tilde{k}_{\mathrm{ss}}(\varphi')\rangle = \sum_{k'}(W_0)_{k,k'}|k'_{\mathrm{ss}}(\varphi')\rangle$ is a rotated basis for the stationary state in the decoder Hilbert space, defined by an arbitrary unitary W_0. The decoder Hilbert space is assumed to have the same dimension as the sensor Hilbert space. The resulting stationary state of the cascaded system is a pure state $|D\rangle = \sum_k \sqrt{p_k}|k\rangle_{\mathrm{S}} \otimes |\tilde{k}\rangle_{\mathrm{D}}$

In the stationary regime ($\omega < \omega_{\mathrm{c}}$) of the BTC, the sensor stationary state is given by a pure coherent state $|E_0\rangle_{\mathrm{S}\,\mathrm{S}}\langle E_0|$ of the sensor jump operator (see Sec. A.6). The transformed state, $|E_0\rangle_{\mathrm{D}}$, of the decoder is a copy of $|E_0\rangle_{\mathrm{S}}$ on the decoder Hilbert space. In such a situation Eq. (A.37) and Eq. (A.38) reduce to the more simple form $\hat{H}_{\mathrm{D}} = -W_0\hat{H}_{\mathrm{S}}(\varphi')W^\dagger_0$ and $\hat{L}_{\mathrm{D}} = -W_0\hat{L}_{\mathrm{S}}(\varphi')W^\dagger_0$, in the

sense that their matrix elements in the state $|E_0\rangle_{\rm S}$ and $|E_0\rangle_{\rm D}$ respectively are identical. With the choice

$$W_0 = \exp\left[i\pi \hat{S}_{\rm z}^{\rm S}\right], \tag{A.39}$$

the operators of the decoder are $\hat{H}_{\rm D} = \omega \hat{S}_{\rm x}^{\rm D}$ and $\hat{L}_{\rm D} = \kappa e^{-i\varphi'} \hat{S}_-^{\rm D}$, with $\hat{S}_\alpha^{\rm D}$ acting on the decoder Hilbert space and $\hat{S}_\alpha^{\rm S}$ on the sensor Hilbert space. This means, that the optimal decoder is an identical copy of the sensor with a phase shift φ' imprinted on emitted photons.

A.5. Construction of the dark state in the cascaded system

The derivation here is analog to [38]. In the special case of Eq. (4.6) $\Delta\varphi = 0$, the dark state conditions reduce to a more simple problem, which can be solved by the theory of angular momentum coupling

$$
\begin{aligned}
&(1) \quad \left(\hat{S}_-^{\rm S} + \hat{S}_-^{\rm D}\right)|D\rangle = 0,\\
&(2) \quad -i\omega[\hat{S}_{\rm x}^{\rm S} + \hat{S}_{\rm x}^{\rm D}, \rho] - \frac{\kappa}{2}[\hat{S}_+^{\rm D}\hat{S}_-^{\rm S} - \hat{S}_-^{\rm D}\hat{S}_+^{\rm S}, |D\rangle\langle D|] = 0.
\end{aligned}
\tag{A.40}
$$

As one can see, the first condition now indicates that the state $|D\rangle$ has to be annihilated by the coupled lowering operator. A solution to these dark state conditions is known [38] and reads

$$|D\rangle = \sum_{J=0}^{2S} A_J(\omega, \kappa)|J, -J\rangle, \tag{A.41}$$

where $|J, -J\rangle$ is a state in the basis of the coupled angular momentum operators $\hat{J}_\alpha = \hat{S}_\alpha^{\rm S} + \hat{S}_\alpha^{\rm D}$

$$|J, -J\rangle \sum_{M_{\rm S}, M_{\rm D}} C_{S,M_{\rm S};S,M_{\rm D}}^{J,-J} |S, M_{\rm S}; S, M_{\rm D}\rangle, \tag{A.42}$$

with the Clebsch-Gordan coefficients $C_{S_1,M_1;S_2,M_2}^{J,M_J}$ and $|S, M_{\rm S}; S, M_{\rm D}\rangle$ denotes a state with z-components M_i of the sensor and decoder momenta, respectively. $S = N/2$ is the total angular momentum of the respective subsystems. Since $\hat{J}_-|J, -J\rangle = 0$ it is straightforward to see, that the dark state condition (1) is satisfied by $|D\rangle$. In order to satisfy the condition (2) as well, the coefficients A_J have to fulfill the following recurrence relation

$$
\begin{aligned}
\omega A_J \sqrt{2J} C_{S,M_{\rm S};S,M_{\rm D}}^{J,-J+1} = i\kappa A_{J-1}[&(1 - \delta_{-S,M_{\rm S}+1})(1 - \delta_{S,M_{\rm D}-1})P_+ C_{S,M_{\rm S}+1;S,M_{\rm D}-1}^{J-1,-J+1}\\
&-(1 - \delta_{-S,M_{\rm D}+1})(1 - \delta_{S,M_{\rm S}-1})P_- C_{S,M_{\rm S}-1;S,M_{\rm D}+1}^{J-1,-J+1}],
\end{aligned}
\tag{A.43}
$$

with the coefficients $P_\pm$ given as $P_\pm = \sqrt{(S \pm M_{\rm S} + 1)(S \mp M_{\rm S})(S \mp M_{\rm D} + 1)(S \pm M_{\rm D})}$. As one can see, this recurrence relation is only valid for $J \in [1, 2S]$ and with the condition $M_{\rm S} + M_{\rm D} = -J + 1$, according to angular momentum coupling theory. This recurrence relation can be solved with the initial condition $A_{2S} = K$. Then one obtains the following expression for the coefficients A_J

$$
\begin{aligned}
A_J &= \left(\frac{\omega}{i\kappa}\right)^{2S-J} a_J K,\\
\Rightarrow \langle D|D\rangle &= \sum_{J=0}^{2S} |A_J|^2 = |K|^2 \left(1 + \sum_{J=0}^{2S-1} \left|\left(\frac{\omega}{i\kappa}\right)^{2S-J}, a_J\right|^2\right) \stackrel{!}{=} 1\\
\Rightarrow |K| &= \left(1 + \sum_{J=0}^{2S-1} \left|\left(\frac{\omega}{i\kappa}\right)^{2S-J} a_J\right|^2\right)^{-1/2},
\end{aligned}
\tag{A.44}
$$

where the a_J are factors only dependent on J and S. In the limit of small driving $\omega \ll \omega_{\rm c}$, the dark state approaches $|D\rangle \to |2S, -2S\rangle$ and for strong driving $\omega \gg \omega_{\rm c}$, it approaches $|D\rangle \to |0, 0\rangle$.

A.6. Holstein Primakoff approach to the cascaded system

In this section, HP approach is taken to the cascaded system, to obtain an analytical expression for the estimation error $\delta\varphi$ in the stationary regime ($\omega < \omega_c$). The derivation is similar to the one in [38] and applies it to the system described in Sec. 4.1. The starting point is the transformation to a bosonic modes for the sensor and decoder respectively

$$\hat{S}^i_+ = \hat{b}^\dagger_i \sqrt{2S - \hat{b}^\dagger_i \hat{b}_i}, \ \hat{S}^{(i)}_- = \sqrt{2S - \hat{b}^\dagger_i \hat{b}_i}\, \hat{b}_i, \tag{A.45}$$

where the index i indicates the operators of the sensor ($i = $ S) and of the decoder ($i = $ D). Assuming a large displaced state, one can shift the bosonic modes to

$$\hat{b}_i \to \hat{b}_i + \sqrt{S}\beta_i, \tag{A.46}$$

where the β_i are complex fields yet to be determined. If S is a large displacement, then $\epsilon = 1/\sqrt{S}$ is a small parameter and one can expand the spin operators

$$\hat{m}^i_\alpha = \frac{\hat{S}^i_\alpha}{S} = \sum_{l=0}^\infty \epsilon^l \hat{m}^i_{\alpha,l}. \tag{A.47}$$

The expansion up to $\mathcal{O}(\epsilon)$ of the operators is given as in the single system case as

$$\hat{m}^i_+ = m^i_{+,0} + \epsilon \underbrace{\frac{1}{2\sqrt{k_i}}[(4 - 3|\beta_i|^2) - |\beta_i|^2)\hat{b}^\dagger_i - \beta^{*2}_i \hat{b}_i]}_{\hat{m}^i_{+,1}} + \mathcal{O}(\epsilon^2), \tag{A.48}$$

where $k_i = 2 - |\beta_i|^2$ and $m^i_{+,0} = \beta^*_i \sqrt{k_i}$. The stationary state can be determined via the reascaled LME

$$\partial_\tau \rho = -iS\tilde{\omega}[\hat{m}^S_x + \hat{m}^D_x, \rho] - \frac{\kappa}{2}S[e^{-i\Delta\varphi}\hat{m}^D_+ \hat{m}^S_- - e^{i\Delta\varphi}\hat{m}^S_+ \hat{m}^D_-, \rho]$$

$$+ \kappa S\mathcal{D}[e^{-i\varphi}\hat{m}^S_- + e^{-i\varphi'}\hat{m}^D_-]\rho \tag{A.49}$$

$$\overset{!}{=} 0,$$

where the rescaled parameters $\omega = S\tilde{\omega}$ and $\tau = St$ as for the single system are used. In order to find the conditions for a stationary state, the density matrix is also expanded as $\rho = \sum_{l=0}^\infty \epsilon^l \rho_l$. Then Eq. (A.49) yields, up to order $\mathcal{O}(\epsilon)$,

$$0 = -i\tilde{\omega} \pm \kappa m^S_{\pm,0} \text{ and } 0 = -\frac{i\tilde{\omega}}{2} \pm \kappa e^{\pm i\Delta\varphi}m^S_{\pm,0} \pm \frac{\kappa}{2}m^D_{\pm,0}, \tag{A.50}$$

which can be solved by

$$m^S_{\pm,0} = \pm\frac{i\tilde{\omega}}{\kappa}, \ \ m^D_{\pm,0} = \pm\frac{i\tilde{\omega}}{\kappa}(1 - 2e^{\pm i\Delta\varphi}). \tag{A.51}$$

From this, one can now determine a solution for the unknown fields β_i

$$\beta_S = -i\sqrt{1 - \sqrt{1 - (\tilde{\omega}/\kappa)^2}}. \tag{A.52}$$

For β_D, one can use the relation

$$m^D_{-,0} = \beta_D\sqrt{2 - |\beta_D|^2} \overset{!}{=} -i\frac{\tilde{\omega}}{\kappa}(1 - 2e^{-i\Delta\varphi})$$

$$\Rightarrow |\beta_D|^2 = 1 - \sqrt{1 - \frac{\tilde{\omega}^2}{\kappa^2}(5 - 4\cos(\Delta\varphi))} \tag{A.53}$$

$$\Rightarrow \beta_D = -\frac{i\tilde{\omega}}{\kappa}\frac{1 - 2e^{-i\Delta\varphi}}{\sqrt{1 + \sqrt{1 - (\tilde{\omega}^2/\kappa^2)(5 - 4\cos(\Delta\varphi))}}},$$

where one can see, that this is only valid in the regime $\tilde{\omega}^2 \leq \kappa^2/(5 - 4\cos(\Delta\varphi))$ or in other terms, one obtains a transition line for the cascaded system along $\omega_{c,casc} = \omega_c/\sqrt{5 - 4\cos(\Delta\varphi)}$, with the single system critical frequency ω_c. The next to leading order term yields

$$\partial_\tau \rho_0 = -\frac{\kappa}{2}[e^{-i\Delta\varphi}\hat{m}^D_{+,1}\hat{m}^S_{-,1} - e^{i\Delta\varphi}\hat{m}^S_{+,1}\hat{m}^D_{-,2}, \rho_0] + \kappa\mathcal{D}[e^{-i\varphi}\hat{m}^S_{-,1} + e^{-i\varphi'}\hat{m}^D_{-,2}]\rho_0$$
$$\overset{!}{=} 0. \tag{A.54}$$

This can be solved by the ansatz

$$\rho_{0,ss} = (|E^S_0\rangle \otimes |E^D_0\rangle)(\langle E^S_0| \otimes \langle E^D_0|), \tag{A.55}$$

with the vacuum of the fluctuations $\hat{m}^i_{-,1}|E^i_0\rangle = 0$. By writing out the fluctuations as $\hat{m}^i_{-,1} = A_i\hat{b}_i + B_i\hat{b}^\dagger_i$ with

$$B_S = -\frac{1 - \sqrt{1 - \tilde{\omega}^2/\kappa^2}}{2\sqrt{k_S}}, \quad A_S = \frac{1 + 3\sqrt{1 - \tilde{\omega}^2/\kappa^2}}{2\sqrt{k_S}}, \tag{A.56}$$

$$B_D = \frac{(-i\tilde{\omega}/\kappa)1 - 2e^{i\Delta\varphi}}{\sqrt{1 + \sqrt{1 - (\tilde{\omega}^2/\kappa^2)(5 - 4\cos(\Delta\varphi))}}\sqrt{2k_D}}, \quad A_D = \frac{1 + 3\sqrt{1 - (\tilde{\omega}^2/\kappa^2)(5 - 4\cos(\Delta\varphi))}}{2\sqrt{k_D}}, \tag{A.57}$$

the explicit form of the stationary state can be determined. Notice that $|B_i/A_i| \leq 1$ and thus one can find the vacuum states of the respective fluctuations

$$|E^i_0\rangle = \frac{1}{\sqrt{\mathcal{N}}}\left(|0\rangle_i + \sum_{n=1}^\infty \left(\frac{-B_i}{A_i}\right)^n \sqrt{\frac{(2n-1)!!}{2n!!}}|2n\rangle_i\right). \tag{A.58}$$

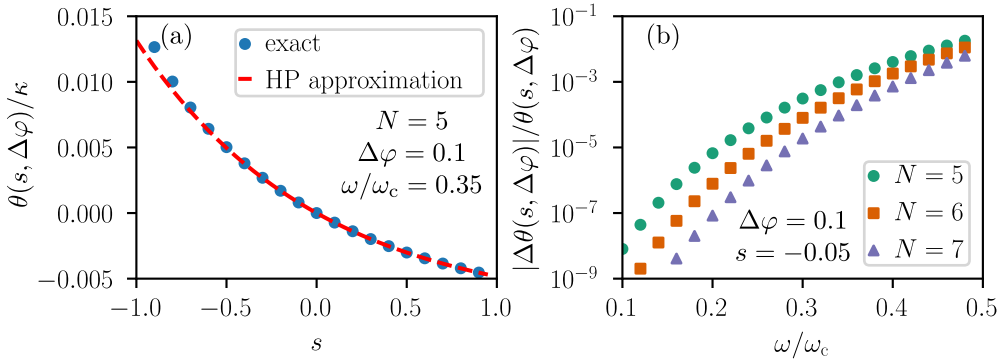**Estimation error for the cascaded protocol**

Figure A.5: **Benchmark for the approximate expression of the cascaded protocol estimation error.** (a) Dominant eigenvalue of Eq. (4.11) as a function of the bias parameter s, for $\Delta\varphi = 0.1$, fixed system size $N = 5$ and in the stationary regime $\omega/\omega_c = 0.35$. The red dashed line is obtained evaluating the result obtained by the HP approach, whereas the blue dots are computed by diagonalization of Eq. (4.11). (b) Relative error of the dominant eigenvalue θ as a function of the Rabi frequency ω, for different system sizes and fixed values $\Delta\varphi = 0.1$ and $s = -0.05$. The error is defined as the absolute difference of the HP approximated value and the and the exact diagonalized value and both divided by the exact value. One observes, that the error increases towards the critical Rabi frequency, but is small in a large portion of the stationary regime. Also one finds an improvement of the approximation with increasing system size.

The estimation error can be determined via the dominant eigenvalue of Eq. (4.11). The evolution of the stationary state $\rho_{0,ss}$ for a small time increment $\Delta\tau$, according to the tilted and rescaled ME is given by

$$\rho(\Delta\tau) = \rho_{0,ss} + \Delta\tau\kappa S(e^{-s} - 1)(e^{-i\varphi}\hat{m}^S_- + e^{-i\varphi'}\hat{m}^D_-)\rho_{0,ss}(e^{i\varphi}\hat{m}^S_+ + e^{i\varphi'}\hat{m}^D_+)$$
$$\approx \rho_{0,ss} + \Delta\tau\kappa S(e^{-s} - 1)(e^{-i\varphi}\hat{m}^S_{-,0} + e^{-i\varphi'}\hat{m}^D_{-,0})\rho_{0,ss}(e^{-i\varphi}\hat{m}^S_{+,0} + e^{i\varphi'}\hat{m}^D_{+,0}), \tag{A.59}$$

where only the dominant terms are taken into account. The dominant eigenvalue in this approximation is thus given by

$$
\begin{aligned}
\theta(s, \Delta\varphi) &\approx \kappa S^2 (e^{-s} - 1)(m_{-,0}^S m_{+,0}^S + m_{-,0}^D m_{+,0}^D + e^{-i\Delta\varphi} m_{-,0}^S m_{+,0}^D + e^{i\Delta\varphi} m_{-,0}^D m_{+,0}^S \\
&= S^2 (e^{-s} - 1)\frac{\tilde{\omega}^2}{\kappa} 2(1 - \cos(\Delta\varphi)) \\
&= 2(e^{-s} - 1)\frac{\omega^2}{\kappa}(1 - \cos(\Delta\varphi)),
\end{aligned}
\tag{A.60}
$$

which is benchmarked with data obtained by diagonalization of Eq. (4.11) in Fig. A.5. From this, one can now compute the estimation error as

$$
\overline{\delta\varphi} = \frac{\sqrt{\partial_s^2 \theta(s, \Delta\varphi)}}{|\partial_\varphi \partial_s \theta(s, \Delta\varphi)|}\Big|_{s=0} = \frac{\sqrt{1 - \cos(\Delta\varphi)}}{\sqrt{2}\frac{\omega}{\sqrt{\kappa}}|\sin(\Delta\varphi)|}.
\tag{A.61}
$$

Mean-field operators for the cascaded system

In this section, the equations of motion for the rescaled operators $\hat{m}_\alpha^N = 2\hat{S}_\alpha/N$ are determined. In the limit $N \to \infty$ these operators converge to multiples of the identity, such that $\lim_{N\to\infty} \hat{m}_\alpha^N = \lim_{N\to\infty} \langle \hat{m}_\alpha^N \rangle =: m_\alpha$ [21, 67, 68]. While the time evolution of the density matrix is given by the LME, the evolution of expectation values is given by an adjoint LME, which reads

$$
\begin{aligned}
\partial_t \langle \hat{m}_\alpha^N \rangle = &- i\omega \langle [\hat{m}_\alpha^N, \hat{S}_x^S + \hat{S}_x^D] \rangle - \frac{\kappa}{2} \langle [\hat{m}_\alpha^N, e^{-i\Delta\varphi} \hat{S}_+^D \hat{S}_-^S - e^{i\Delta\varphi} \hat{S}_+^S \hat{S}_-^D] \rangle \\
&+ \kappa \langle (e^{i\varphi} \hat{S}_+^S + e^{i\varphi'} \hat{S}_+^D) \hat{m}_\alpha^N (e^{-i\varphi} \hat{S}_-^S + e^{-i\varphi'} \hat{S}_-^D) \\
&- \frac{1}{2} \{ (e^{i\varphi} \hat{S}_+^S + e^{i\varphi'} \hat{S}_+^D)(e^{-i\varphi} \hat{S}_-^S + e^{-i\varphi'} \hat{S}_-^D), \hat{m}_\alpha^N \} \rangle.
\end{aligned}
\tag{A.62}
$$

Using the respective commutation relations and the rescaling $\omega_c = 2\kappa/N$, one can thus obtain the following equations of motion for the rescaled operators in the limit $N \to \infty$

$$
\dot{m}_x^S = \omega_c m_x^S m_z^S
\tag{A.63}
$$

$$
\dot{m}_y^S = -\omega m_z^S + \omega_c m_y^S m_z^S
\tag{A.64}
$$

$$
\dot{m}_z^S = \omega m_y^S - \omega_c \left((m_x^S)^2 + (m_y^S)^2\right)
\tag{A.65}
$$

$$
\dot{m}_x^D = \omega_c (m_x^D m_z^D + 2 m_x^S m_z^D \cos(\Delta\varphi) - 2 m_y^S m_z^D \sin(\Delta\varphi))
\tag{A.66}
$$

$$
\dot{m}_y^D = -\omega m_z^D + \omega_c (m_z^D m_y^D + 2 m_x^S m_z^D \sin(\Delta\varphi) + 2 m_y^S m_z^D \cos(\Delta\varphi))
\tag{A.67}
$$

$$
\begin{aligned}
\dot{m}_z^D = &\omega m_y^D - 2\omega_c (m_x^S m_x^D \cos(\Delta\varphi) + m_y^S m_y^D \cos(\Delta\varphi) \\
&+ m_x^S m_y^D \sin(\Delta\varphi) - m_y^S m_x^D \sin(\Delta\varphi)) - \omega_c ((m_x^D)^2 + (m_y^D)^2).
\end{aligned}
\tag{A.68}
$$

As can be seen in the LME, the operators $(\hat{S}^i)^2$ commute with all operators determining the time evolution, meaning that the expectation values $\langle (\hat{S}^i)^2 \rangle$ are conserved and thus as well the quantities $(m^i)^2 = (m_x^i)^2 + (m_y^i)^2 + (m_z^i)^2$ are conserved. With the initial condition $(\hat{S}^i)^2 = N/2$, this means that $(m^i)^2 = 1$ is constant. These equations in the thermodynamic limit determine the values of $m_\pm^i$. In the stationary regime and one can compare them with the values obtained in the Holstein-Primakoff approach. One finds

$$
0 = m_x^S, \ m_y^S = \frac{\omega}{\omega_c} \Rightarrow m_\pm^S = \pm i \frac{\omega}{\omega_c},
\tag{A.69}
$$

for the sensor and for the decoder

$$
0 = \omega_c \left(m_x^D - 2 m_y^S \sin(\Delta\varphi) \right) \Rightarrow m_x^D = 2 \frac{\omega}{\omega_c} \sin(\Delta\varphi)
\tag{A.70}
$$

$$
\omega = \omega_c \left(m_y^D + 2 \frac{\omega}{\omega_c} \cos(\Delta\varphi) \right) \Rightarrow m_y^D = \frac{\omega}{\omega_c}(1 - 2\cos(\Delta\varphi))
\tag{A.71}
$$

$$
\Rightarrow m_\pm^D = \frac{\omega}{\omega_c}(2\sin(\Delta\varphi) \pm i \mp 2i\cos(\Delta\varphi)) = \pm i \frac{\omega}{\omega_c}(1 - 2e^{\pm i\Delta\varphi}),
\tag{A.72}
$$

which agrees with the results for $m_{\pm,0}^i$ in Eq. (A.50).

Acknowledgements

First and foremost, I thank my two supervisors, Prof. Dr. Igor Lesanovsky and Dr. Albert Cabot who gave me the opportunity to work on this fascinating research topic. I highly value the knowledge gained and feedback obtained throughout the work on this thesis and the discussion of its results. Your guidance was an inspiration for me.

I would also like to express my gratitude to all the members of the Bachelor office, with whom I had many inspiring discussions. The collective lunches and pull-up sessions provided great motivation during the writing of this thesis.

Contact Information

Malik Jirasek
Institut für Theoretische Physik
Auf der Morgenstelle 14
Universität Tübingen
72076 Tübingen
malik.jirasek@student.uni-tuebingen.de